


Information-driven robotic sampling in the coastal ocean

Trygve Olav Fossum^{1,2}  | Jo Eidsvik³ | Ingrid Ellingsen⁴ | Morten Omholt Alver⁴ |
 Glauca Moreira Fragoso⁵ | Geir Johnsen^{2,5,6} | Renato Mendes^{7,8,9} |
 Martin Ludvigsen^{1,2,6} | Kanna Rajan^{2,7,10}

¹Department of Marine Technology, Norwegian University of Science and Technology (NTNU), Trondheim, Norway

²Centre of Autonomous Marine Operations and Systems (AMOS), Trondheim, Norway

³Department of Mathematical Sciences, Norwegian University of Science and Technology (NTNU), Trondheim, Norway

⁴SINTEF Ocean AS, Trondheim, Norway

⁵Department of Biology, Norwegian University of Science and Technology (NTNU), Trondheim, Norway

⁶University Centre in Svalbard (UNIS), Longyearbyen, Norway

⁷Underwater Systems and Technology Laboratory, Faculty of Engineering, University of Porto (UP), Portugal

⁸Interdisciplinary Center for Marine and Environmental Research (CIIMAR), UP, Portugal

⁹Physics Department, CESAM, University of Aveiro, Portugal

¹⁰Department of Engineering Cybernetics, Norwegian University of Science and Technology (NTNU), Trondheim, Norway

Correspondence

Trygve Olav Fossum, Department of Marine Technology, Norwegian University of Science and Technology (NTNU), Otto Nielsens Veg 10, NO-7491, Trondheim, Norway.
 Email: trygve.o.fossum@ntnu.no

Funding information

Nansen Legacy Program, Grant/Award Number: 27272; Senter for Autonome Marine Operasjoner og Systemer, Grant/Award Number: 223254; Norges Forskningsråd, Grant/Award Number: 255303/E40; European Union's Seventh Framework Programme (FP7/2007–2013), Grant/Award Number: 270180

Abstract

Efficient sampling of coastal ocean processes, especially mechanisms such as upwelling and internal waves and their influence on primary production, is critical for understanding our changing oceans. Coupling robotic sampling with ocean models provides an effective approach to adaptively sample such features. We present methods that capitalize on information from ocean models and in situ measurements, using Gaussian process modeling and objective functions, allowing sampling efforts to be concentrated to regions with high scientific interest. We demonstrate how to combine and correlate marine data from autonomous underwater vehicles, model forecasts, remote sensing satellite, buoy, and ship-based measurements, as a means to cross-validate and improve ocean model accuracy, in addition to resolving upper water-column interactions. Our work is focused on the west coast of Mid-Norway where significant influx of Atlantic Water produces a rich and complex physical–biological coupling, which is hard to measure and characterize due to the harsh environmental conditions. Results from both simulation and full-scale sea trials are presented.

KEYWORDS

Gaussian processes, marine robotics, ocean modeling, ocean sampling, robotic sampling

1 | INTRODUCTION

The coastal waters (CWs) of Middle Norway, and the Froan archipelago is influenced by Atlantic Water (AW),* local water masses from the Trondheim Fjord (FW), and CW transported by Norwegian coastal current (NCC; Sætre, 2007). The elevated levels of mixing that occur

increase the nutrient transport necessary for primary production—the main source of energy and basis for the marine food web. In addition to the influx of AW, complex coastal topography makes the region exceptionally productive and important in terms of marine life and biodiversity, with a broader ecological, scientific, and social-economical significance (Sætre, 2007). Despite this, little is known about the basic

This is an open access article under the terms of the Creative Commons Attribution-NonCommercial License, which permits use, distribution and reproduction in any medium, provided the original work is properly cited and is not used for commercial purposes.

© 2018 The Authors. *Journal of Field Robotics* published by Wiley Periodicals, Inc.

* AW is defined by a salinity ≥ 35.0 and temperature $>3^\circ\text{C}$, CW has a salinity ≥ 34.7 and a wider temperature range (Sakshaug, Johnsen, & Kovacs, 2009), while FW is related to salinities below 34.7.

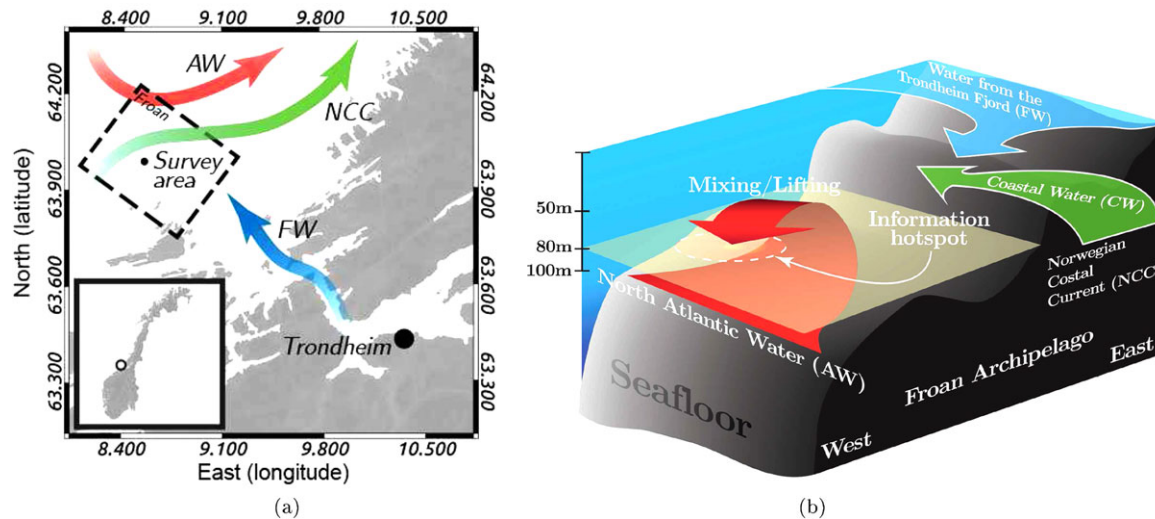


FIGURE 1 (a) The Middle-Norway coastal region and the Froan archipelago. The location of the survey area and its relation to the Norwegian coastline (inset). (b) The physical driving forces in the Froan area, the coastal region of investigation. The convergence of different currents at the Froan archipelago, where influx of Atlantic Water (AW) is predicted to provide nutrient rich deep water, which accentuates primary productivity. In order to understand the region's significance it is essential to sample this influx, which is an "information hotspot"

driving mechanisms and their effect on the marine ecosystem (Asplin, Salvanes, & Kristoffersen, 1999). The spatial and temporal scales of ocean processes make it unrealistic to deploy vast resources to record these dynamics in detail. Consequently, the use of ocean models to represent the dynamics is critical for realizing sampling strategies that return information with high scientific quality. Together with the complex bio-geophysical interactions involved, this forms the motivation for the development of information-driven sampling strategies, which is the focus of this paper.

With the increasing availability of high-end computational resources accessible to oceanographers, multiresolution modeling of the upper water-column, for predictive or post hoc purposes, has been a new and viable tool to understand complex interactions between physical and biological features. However, modeling skill is still at a level where physical, biological, and chemical features related to ocean structure and circulation cannot be used to make accurate predictions at scales sufficient for definite representation (Lermusiaux, 2006). To understand these upper water-column biogeochemical processes, scientists have to resort to direct observations (Stewart, 2009), which are typically sparsely distributed in both time and space leading to *undersampling*. Making intelligent and targeted observations is therefore becoming exceedingly important for oceanography, which is an expensive and demanding enterprise, restricted to static sensors placed on buoys, or measurements taken by personnel on ships.

Recently, mobile robotic platforms, such as autonomous underwater vehicles (AUVs), have become more affordable, robust and viable for scientific exploration, with greater functionality, increased scientific payload, and in-water duration, providing an efficient platform for autonomous collection of in situ oceanographic data.

Increasingly, ocean models and AUVs are being combined to address this common problem of undersampling and uncertainty. We describe one methodology involved in combining these resources toward developing sampling methods that can capitalize on the expressiveness of the model and in situ information. Having access to both

prior (model) and current (sensor) information, AUVs can operate on an a posteriori knowledge, allowing execution to be adjusted according to the geographical context and the upper ocean feature(s) of interest. This leads to a sampling strategy that can both improve model accuracy and exceed traditional approaches in locating and mapping oceanographic phenomena. To support and verify such an approach, data inputs from multiple sources, including remote sensing satellite data, ship-based measurements, near real-time data from buoys, drifters, and other robotic platforms are necessary. This in turn enables cross-verification, assimilation, and adjustment of model parameters, as well as analysis of AUV performance.

The unification of models, remote sensing resources, and different robotic elements is essential in order to increase the predictive power of models for effective autonomous ocean sampling. Our work is motivated from campaigns such as the Autonomous Ocean Sampling Network (AOSN-I/-II; Curtin, Bellingham, Catipovic, & Webb, 1993; Ramp et al., 2009), and the Controlled Agile and Novel Observation Network (CANON) field program (Das et al., 2010, 2012), both from Monterey Bay, California. It brings together biological and physical oceanography with autonomous robotic control while providing focus on the Froan archipelago, located outside the CWs of Middle Norway, see Figure 1. In addition to AUVs, data were collected from satellites, buoys, surface autonomous platforms (WaveGlider[†]), and ship-based surveys, primarily as a means to ground truth in situ robotic data. Data collection in the Froan area is particularly challenging due to inclement weather, narrow straits, complex bathymetry, and its remote location. An overview of the system setup for the campaign is shown in Figure 2.

The paper is organized as follows. Section 2 provides the context of this work in relation to other efforts. Section 3 provides definitions and reviews background information on ocean sampling, modeling, methods, and data assimilation. Section 4 is the core of our paper

[†] The WaveGlider and payload storage was damaged upon recovery, and is therefore not included in this work.

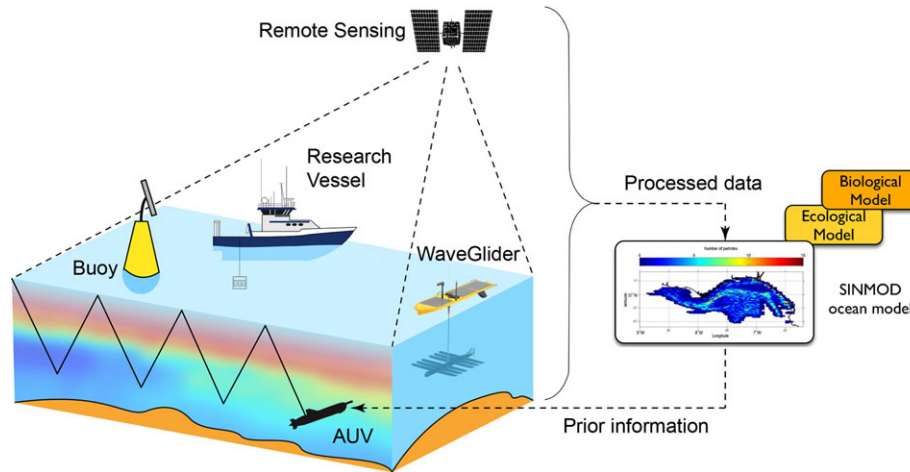


FIGURE 2 System block diagram of the platforms used in the sampling campaign: Ocean model SINMOD, moored buoy (temperature, salinity, and biological measurements), research vessel (biological and physical measurements), remote sensing (temperature and chlorophyll *a*), autonomous surface vehicle (temperature, salinity, and weather data), and an AUV (biological and physical measurements)

and articulates the approach and the specific algorithm we have developed. Section 5 provides an in-depth perspective on the field experiments and the subsequent analysis from various data sources. Finally, Sections 6 and 7 conclude with a summary discussion, conclusions, and future work.

2 | RELATED WORK

Our work is related to informative sampling strategies and autonomous data collection in the ocean. There is a large body of literature on maximizing information gain from in situ measurements to characterize phenomena, or providing estimation of a scalar field. Zhang and Sukhatme (2007) showed adaptive sampling schemes for reconstructing a temperature field using a sensor network of both static and mobile sensors, while Graham et al. (2012) discussed the use of Gaussian processes (GPs) and the problems relating to environment reconstruction in the ocean with different correlation kernels. Yilmaz, Evangelinos, Lermusiaux, and Patrikalakis (2008) used a mixed integer programming utility combining reduction of uncertainty and physical constraints. Chekuri and Pal (2005) optimized informative paths using a recursive greedy approach with mutual information in directed graphs. Although adaptation is not the focus, the authors explore the utility of sampling a dynamic field in space and time. This concept is further studied for an application with multiple robots in Singh, Krause, Guestrin, and Kaiser (2009). Minimizing estimation error of a sampled field using optimal distribution of mobile sensors in the ocean is presented in Leonard et al. (2007). Low et al. (2011) discussed efficient information-theoretic path planning for sampling of GP-based fields using a Markov policy based on entropy, with empirical results on real-world temperature and plankton density field data. This is expanded to include anisotropic fields in Cao, Low, and Dolan (2013). Nonparametric optimization is explored in Zamuda, Hernandez Sosa, and Adler (2016), where a self-adaptation path planning scheme for a glider is developed for exploration of submesoscale eddies.

Ocean models are used to estimate the underlying current field toward improving energy efficiency and navigation for AUVs and glid-

ers in Chang, Zhang, and Edwards (2015) and Rao and Williams (2009). Statistical estimation of surface currents using satellite data have also been suggested as an effective aid for handling dynamics in Frolov, Paduan, Cook, and Bellingham (2012). Online algorithms and decision strategies can also be trained and tuned using ocean models and Markov decision processes, and have been applied to AUVs influenced by spatial and temporal uncertainty in Ma, Liu and Sukhatme (2016). In situ identification of features using GP regression and supervised learning is presented in Das et al. (2015), with the aim to select optimal sampling points, for an AUV with water sampling capabilities. Similar approaches are also used in Bayesian optimization, where for instance Marchant et al. (2014) formulate a Monte Carlo tree search for robot path planning. Ling, Low, and Jaillet (2016) have developed an approximate dynamic programming approach in a similar vein, where the reward function includes the posterior mean and not only variance terms (which do not depend on the data).

The work presented here is also associated with sensor placement problems that have been explored for GPs in Guestrin, Krause, and Singh (2005), Krause, Guestrin, Gupta, and Kleinberg (2006), and Krause, Singh, and Guestrin (2008) who use a greedy algorithm for maximizing mutual information. Coupling adaptation and modeling is studied in Smith et al. (2010, 2011), Smith, Py, Cooksey, Sukhatme, and Rajan (2016) employing prior information from ocean models and adaptive approaches for the characterization of a frontal system and sampling phytoplankton blooms. Binney, Krause, and Sukhatme (2010) use the measure of *mutual information* and Gaussian approximation techniques to relate the sampled and unsampled locations, optimizing information gain along a 2D path for a glider. This is further elaborated considering time variation with a surface vehicle in Binney, Krause, and Sukhatme (2013).

Our work presents an end-to-end, real-world implementation, of an information-theoretic sampling system for environmental sensing of the upper water-column that combines information from ocean models and in situ measurements, using a balance between variance and gradient based measures. We show how integration and utilization of ocean model data can be leveraged in GP modeling and used for

directing sampling efforts to regions of high scientific interest. Specifically, this involves modifying the probabilistic model using data to develop a nonstationary correlation kernel and a bias correcting mean. Finally, we present experimental validation and correlation with other marine data.

3 | BACKGROUND

3.1 | The SINMOD ocean model

Ocean models describe the state of the ocean at a given time based on a set of hydrodynamic and thermodynamic equations, commonly called the *primitive equations*, that are solved using numerical techniques. These equations provide information about currents, salinity, temperature, density, and pressure. In implementations, the equations are discretized in different ways, utilizing either structured or unstructured model grids horizontally, and using horizontal terrain-following or hybrid discretization vertically. The spatial resolution of an ocean model represents a trade-off between the geographical area to be simulated and the availability of computer hardware and time. Running the model involves computation of a large number of equations, typically implemented with parallelization in order to utilize more CPUs to reduce computing time. Because high-resolution modeling can only be done for relatively small geographical areas, models are commonly nested, that is, one simulates larger scale areas to produce boundary conditions for higher resolution models covering smaller areas. This process can be iterated several times, to achieve the desired detail. Models apply forcing by tides, sea-level pressure, wind, heat exchange, and freshwater runoff. Regional models additionally need prescribed states and currents at the open boundaries. Errors in the forcing data also impact the quality of the model output. This can typically be the accuracy of wind fields in coastal areas with strong topographic steering of near-surface wind. The quality of bathymetric data, type of grid used, and choice of numerical techniques are other factors that influence ocean model output.

Model performance can be evaluated using observations from different platforms such as AUVs, buoys, or ship-based sampling. Due to the chaotic nature of the processes in the upper water-column, the scale and accessibility of the ocean makes it difficult to obtain sufficient measurements, both for validation purposes and for model correction. In addition to hindcast model validation and correction, information from in situ instrumentation can also improve the near-real-time forecast using persistent data assimilation into the oceanic model. Surface data are usually assimilated in operational models, mostly from satellite imagery. With advancing technology, AUVs will likely play an essential role in the process of data assimilation of water-column properties in such models. AUV data could also be assimilated into predictive models to reduce uncertainties, and in turn be used to guide subsequent AUV missions, thus closing the loop from measurements to modeling and back again (Howe et al., 2010). As shown by validation studies, for example, Forristall (2011), ocean models generally perform well with regard to statistical properties and tidal dynamics, while they show little skill in predicting currents from hour to hour

in areas not dominated by tidal forces. There is therefore a need to develop enabling technology that performs efficient and targeted sampling of the ocean. Robotic methods in sampling are therefore critical for assessing model accuracy and shortcomings, as well as reducing environmental uncertainty and characterization.

SINMOD is a coupled 3D hydrodynamic and biological model system (Slagstad & McClimans, 2005; Wassmann, Slagstad, Riser, & Reigstad, 2006). Its hydrodynamic component is based on the primitive equations that are solved using finite difference techniques using a z-coordinate regular grid with square cells. The model has been used for ocean circulation and ecosystem studies along the Norwegian coast and in the Barents Sea (Wassmann, Slagstad, & Ellingsen, 2010; Ellingsen, Slagstad, & Sundfjord, 2009; Skarøhamar, Slagstad, & Edvardsen, 2007), in ecosystem risk assessment studies (Broch et al., 2013), kelp cultivation potential (Broch, Slagstad, & Smit, 2013) and in climate change effect studies (Ellingsen, Dalpadado, Slagstad, & Loeng, 2008; Slagstad, Wassmann, & Ellingsen, 2015).

In addition to forecasts, SINMOD is capable of providing hindcast and short-term predictions (nowcasts) up to 48 hr. The term *hindcast* is used to describe an after-the-fact analysis or resimulation, where initial conditions, and other model inputs are taken from actual observations. For the production of forecast and nowcast data for the Frøya and Froan region, SINMOD has been set up in a 160-m resolution mode using boundary conditions computed from the operational coastal model system Norkyst800[‡] run by the Norwegian Meteorological Institute (MET).[§] This is a configuration with the Regional Ocean Model System ocean model (Shchepetkin & McWilliams, 2005) for the Norwegian coast with a horizontal resolution of 800 m (Albretsen, 2011). Additionally, SINMOD uses atmospheric input from MEPS 2.5 (Müller et al., 2017) operational weather forecast, by MET (2.5 km horizontal resolution), as well as climatological data for freshwater runoff. For our sampling area in the Froan archipelago, the boundary conditions mediate the tidal circulation and the regional features such as the NCC. They determine the fluxes into and out of the model area, and thereby have a strong influence on model values computed within the area. A snapshot of evolving current speed is shown in Figure 3 as an example of model output.

3.2 | Ocean sampling

Sampling in the ocean is subjected to a broad range of spatial and temporal (including episodic) variability. Often, it is not possible to examine the entire environment in detail, and only a quasi-synoptic (i.e., a non-holistic recording of an event) coverage is possible. This is the sampling problem in oceanography and the lack of sufficient observations is the largest source of error in our understanding (Stewart, 2009), making *when and where* to sample the key problem for designing oceanographic experiments.

Addressing these questions requires a detailed and holistic perspective of the ocean and the interacting processes within. Field experiments, when augmented by ocean models, such as SINMOD, can be

[‡] <https://goo.gl/H4Rbw2>.

[§] <https://www.met.no>.

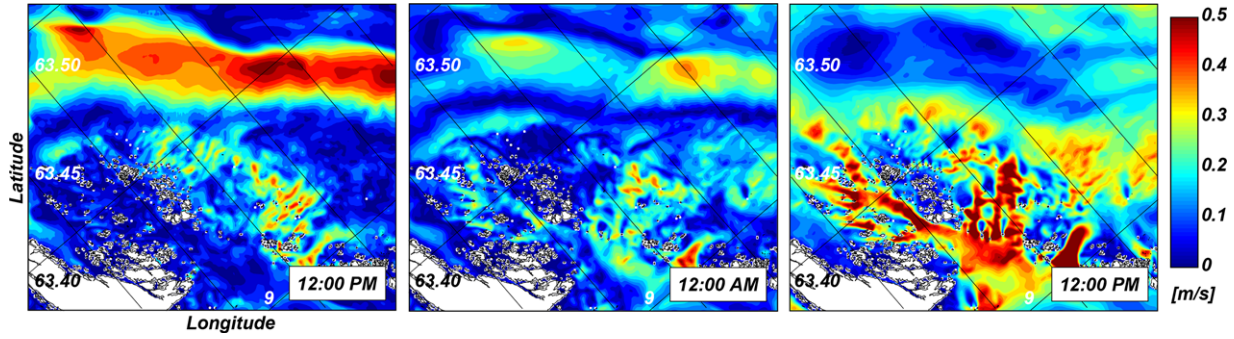


FIGURE 3 Snapshots of typical ocean surface current speeds in the Frøya–Froan region from SINMOD forecasts (nowcasts) from the 5th to 6th of May 2017

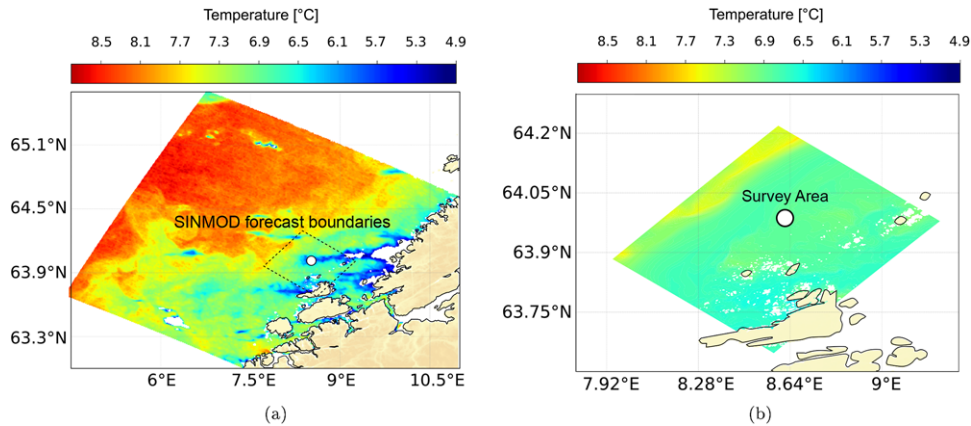


FIGURE 4 L2 products from MODIS-Aqua (<https://oceancolor.gsfc.nasa.gov/>, $1 \times 1 \text{ km}^2$ resolution) for our operational area in the Frøya–Froan region. (a) Sea surface temperature (SST) from Mid-Norway on May 5 at 02:55 a.m. SINMOD SST forecast at 03:00 a.m. The operational area in satellite images is often affected by cloud cover, masking the true underlying ocean temperature

used to simulate, analyze, and plan sampling strategies prior to full-scale deployment. By doing so, sampling resources can target the phenomenon, or the area, of interest in sufficient detail with appropriate sensors. However, numerical ocean models suffer from several sources of errors: practical simplifications, inexact representations or parameterizations, numerical implementations (Lermusiaux, 2006), and the inability to resolve subgrid features, that is, treatment of turbulent dynamics (Troccoli, 2003). This prompts the need for in situ measurements and direct characterization to augment and cross-validate predictions.

Sampling the ocean environment and the latent ecosystem is therefore ideally a joint effort between a range of sources, much as we do in this work, as coincident information about physical (i.e., temperature, salinity, and currents) and biological variables (i.e., light regime, fluorescence, and plankton species) can span multiple temporal and spatial scales. Remotely sensed satellite data can provide repeated large-scale surface observations, such as sea surface temperature (SST), as illustrated in Figure 4, and products of chlorophyll *a* concentration—which represents a phytoplankton biomass indicator. SST satellite products are measured by infrared radiometers over the surface skin layer of the ocean (i.e., $<1 \text{ mm}$ thick). The temperature of this skin layer is often cooler than the body of water below commonly measured by in situ instruments due to heat flux, with the direction of flux typically from the ocean to the atmosphere. The gradients between these

layers are highly dependent on meteorological conditions (Minnett & Kaiser-Weiss, 2012). The spatial resolution is rarely below $1 \times 1 \text{ km}$ in ocean-oriented remote sensing data such as from NASA's MODIS-Aqua (Savtchenko et al., 2004) and about $300 \times 300 \text{ m}$ in the Sentinel-3 constellation mission as part of ESA's Copernicus program (Donlon et al., 2012). Ocean color based products, such as chlorophyll *a*, are calculated using an empirical relationship derived from in situ measurements of chlorophyll concentration and remote sensing reflectances in the blue-to-green region of the visible spectrum. The spatial resolution of the standard chlorophyll products has the same order of magnitude as SST. However, it is possible to derive chlorophyll information from new satellite terrestrial oriented missions as Landsat-8 (OLI sensor) and Sentinel-2 (MSI sensor), which provide data at more relevant spatial scales of 10–60 m (Vanhellemont & Ruddick, 2016). Ocean color satellite data do not cover the water column beyond the first optical attenuation length as defined by Beer's Law, where 90% of remotely sensed radiance originates from (Werdell & Bailey, 2005); this can be too coarse for critical biophysical ocean processes (Moses, Ackleson, Hair, Hostetler, & Miller, 2016). Further, optical remote sensing observations are highly susceptible to cloud cover for certain measurements.

Traditional techniques, like shipboard and moored measurements, can be effective at large spatial ($\text{O}(100 \text{ km})$) and temporal ($\text{O}(\text{week to months})$) scales, but have proved difficult for submesoscale (smaller

than an internal Rossby radius of ($O(10 \text{ km})$) variability (Graham et al., 2012). The importance of these dynamics for physical ocean processes is significant (Barth, Hebert, Dale, & Ullman, 2004) and directly influences primary production (Lévy, 2003) and patch formation (Franks, 1992) of biological signatures.

The use of autonomous and adaptive capabilities allows for responsiveness to interactions as they occur, the opportunity to alter the sampling strategy based on the data available, as well as the sampling resolution in regions of high interest. These factors coupled with the *gaps in observations*, left by other marine data sources, have made marine robotic platforms an integral part of ocean observation.

3.3 | Spatial models and gaussian processes

A prerequisite for doing adaptation and to determine suitable future actions is to have information about the spatial conditions in the area of interest, especially in dynamic environments. Having a high-fidelity numerical ocean model operating onboard a robotic platform is currently infeasible, as the required numerical resolution in both time and space translates into high computational demands. To overcome this problem, a stochastic surrogate model (also known as a proxy or a reduced order model) based on GPs can be used. Apart from having a smaller computational footprint, GPs are conventional tools for dealing with statistical modeling of spatial data and have been widely adopted in oceanographic applications (Binney et al., 2013).

A GP is in essence a collection of random variables that have a *multivariate normal probability density function*. When variables are allocated to spatial locations, a GP is a model that allows spatial dependence to be modeled using covariance functions. Due to its representational flexibility, it is often a popular way to represent environmental processes (see, e.g., Banerjee, Carlin, and Gelfand, 2014; Cressie & Wikle, 2011). Formally

Consider a real-valued stochastic process $\{X(s), s \in \Omega\}$, where Ω is an index set where $\Omega \subset \mathbb{R}^2$. This stochastic process is a GP if, for any finite choice of n distinct locations $s_1, \dots, s_n \in \Omega$, the random vector $\mathbf{x} = [x(s_1), \dots, x(s_n)]$ has a multivariate normal probability density function:

$$p(\mathbf{x}) = N(\boldsymbol{\mu}, \boldsymbol{\Sigma}) = \frac{1}{(2\pi)^{\frac{n}{2}} |\boldsymbol{\Sigma}|^{\frac{1}{2}}} e^{-\frac{1}{2}(\mathbf{x}-\boldsymbol{\mu})^T \boldsymbol{\Sigma}^{-1}(\mathbf{x}-\boldsymbol{\mu})}, \quad (1)$$

defined by the mean vector $\boldsymbol{\mu} = E(\mathbf{x})$, and the symmetric positive definite covariance matrix $\boldsymbol{\Sigma} = \text{cov}(\mathbf{x}, \mathbf{x})$.

The popularity of GPs is often attributed to two essential properties. First, as shown in Equation 1, they can be fully expressed using only a *mean* and a *covariance function* (also known as a *kernel*). This alleviates model fitting, as only the first- and second-order moments need to be specified (Davis, 2014). Second, the procedure for prediction and assimilation is inherent to the fundamental equations of the model, making this step uncomplicated once the GP is formulated. Furthermore, as long as it is possible to estimate the covariance function, a GP can be used on the basis of sparse prior data. In environmental applications, a GP typically characterizes random variation at points in space,

time, or both, discretized down to a grid map with a certain spatiotemporal resolution.

The focus of the statistical model applied in this work is to approximate the underlying distribution of ocean temperature, specified from hindcast data from SINMOD. Using a GP to model temperature as a spatial phenomenon has been studied before (e.g., Cressie & Wikle, 2011; Graham et al., 2012). Based on the characteristics of our ocean model data, the GP is a reasonable model to use for temperatures, as no heavy tails or skewness was significant in the temperature data used for modeling. Furthermore, the GP we use here has a random bias parameter that allows the entire temperature field to be corrected up or down to account for errors in the priors, more details are given in Section 4.1. Such hierarchical GPs (Banerjee et al., 2014) can be useful for adding flexibility in modeling, and therefore viable as a primary building block. The motivation for using temperature is related to a number of factors, which are explained in detail next.

3.4 | Temperature as an information utility

In addition to salinity (S), water temperature (T) plays an outsize role in a variety of oceanographic processes. Together, they provide a strong coupling between physical and biological factors, which are at the heart of the marine life-cycle. In addition, T can be cross-validated using remote sensing data. Physical phenomena such as upwelling, vertical mixing, eddies, fronts, and currents can coincide with temperature variation and gradients (Sverdrup, Duxbury, & Duxbury, 2006), as well as the distribution and accumulation of biological activity (Gordoa, Masó, & Voges, 2000). For example, high variability in T would be visible in frontal zones, where having a T front gliding by a Lagrangian point, would result in a greater gradient in T compared to a region with more stable dynamic conditions. Consequently, T and S play a central role in ocean models, and their broad influence as physical parameters on these nonlinear processes makes them a useful tool for exploring the model error (Holt, Allen, Proctor, & Gilbert, 2005). Using T and S to guide robotic data collection is not new (see, e.g., Zhang, Sukhatme, and Requicha, 2004; Smith, Py, Cooksey, Sukhatme, and Rajan, 2016).

Off the Froan archipelago, results from SINMOD show a combination of stratified and mixed waters, with periodic mixing and lifting of warm and dense AW (Figure 5), creating underwater fronts with higher T gradients, most prominent at 70–90 m depth. The sampling strategy was therefore to concentrate on data collection from this zone with the assumption that the temperature at these depths would be fairly homogeneous, except in areas influenced by AW. Lifting and mixing of AW is important not only for primary productivity, as the AW brings nutrient rich waters to the euphotic zone (0–75 m), but also for the structure and function of the ecosystem. The local bathymetry in the area results in narrowing and strengthening of the NCC outside the Froan archipelago (Sætre, 2007). In combination with high internal wave activity modeled by SINMOD, this results in a dynamic environment and with high variability in S and T, making these *information hot spots* for ocean scientists.

These complex dynamics make the area challenging to model and thus highly relevant for assessing model accuracy. Further, strong dynamics are usually hard to model, especially at smaller scales, and

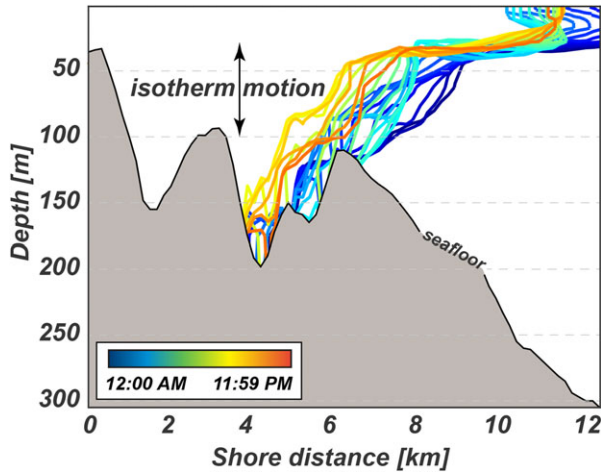


FIGURE 5 Atlantic Water 6.8 °C thermal contour (isotherm) motion from SINMOD simulations, showing the interface shift at the Froan archipelago, for a 24-hr period for May 5th. Note the isotherm shift from 70 to 90 m consistent with our assumptions for data assimilation (see Section 4.2)

resolving sharp temperature gradients is challenging in ocean models (Trenberth, 1992). Sampling the water structure and associated temperature dynamics would, therefore, augment the model and in addition provide vital phenomenological context.

4 | METHODS

Coupling sampling with model-derived information is necessary to improve the capability to study and understand ocean processes that involve physical and biological interactions. Our comprehension of biogeochemical interactions in the upper ocean is, to a large extent, dependent on how ocean models render related processes. Exploring sampling from an ocean model perspective requires us to focus on model shortcomings and inaccuracies, in addition to in situ measurements. The method below is motivated by the characteristics for the Froan archipelago, with temperature as the primary variable of focus for the sampling strategy. However, the approach is general in nature, with a pipeline that can be used to approach sampling, while leveraging data from an ocean model. The following section articulates the approach starting with (a) the discretization and spatial modeling of the phenomena using model data, (b) formulation of the objective function toward a scientific context, and (c) algorithmic implementation. The approach presented here is a *greedy/best-first* search, using a one-node horizon, that is, the method is myopic. This is assumed to be sufficient as the model data have substantial uncertainty that is inherited by the sensing strategy. Moreover, due to control, actuation, and navigational errors in part due to ocean currents, the position of the AUV will deviate from any “optimal” route—a more detailed discussion about myopic versus nonmyopic approaches are given in Section 6.

4.1 | Gaussian process specification

Referring to the definition given in Equation 1, the prior mean $\mu = [\mu_1, \dots, \mu_n]$ is established by simply extracting the statistical mean

temperature for each location $i = 1, \dots, n$. In our case, the data used are a 160-m resolution SINMOD hindcast data set from May 2016, taken at the planned deployment time (~10 a.m.) as

$$\mu_i(\beta_0) = \frac{1}{m} \sum_{j=1}^m x_{ij} + \beta_0 = \bar{x}_i + \beta_0, \quad (2)$$

where x_{ij} is the temperature at location i for the current day j , m is the number of days evaluated from the model, and β_0 is a bias correction term, enabling the AUV to, in situ, correct the prior mean toward the true underlying temperature field, based on the first measurements. As the GP is specified in two dimensions, the mean values constitute a 2D temperature surface. Correction of this surface, using a bias term, allows the AUV to shift all temperatures in unison toward the true mean ocean temperature. The covariance matrix Σ is given as

$$\Sigma = \begin{bmatrix} \Sigma_{11} & \Sigma_{12} & \dots & \Sigma_{1n} \\ \Sigma_{21} & \Sigma_{22} & \dots & \Sigma_{2n} \\ \vdots & \vdots & \ddots & \vdots \\ \Sigma_{n1} & \Sigma_{n2} & \dots & \Sigma_{nn} \end{bmatrix},$$

where $\Sigma_{ij} = \sigma_i \sigma_j \mathcal{K}(i, j)$. Normally, the variance terms σ_i^2 and σ_j^2 are taken to be the same for all locations and collected as σ^2 , making the covariance independent of location (i.e., stationary). Following Stein (2005), these variances are augmented further to include a spatially varying local variance to better suit the local variability—doing so makes measurements at high variance locations have less influence on neighboring locations. We then define the spatially varying variance as

$$\sigma_i^2 = \frac{1}{m} \sum_{k=1}^m (x_{ik} - \bar{x}_i)^2, \quad (3)$$

where x_{ik} is the temperature at location i for the current day k and \bar{x}_i is the average temperature for location i . We used the same 160-m resolution SINMOD hindcast temperature data from May 2016, to calculate the local temperature variance for the survey area. The kernel function is defined as

$$\mathcal{K}(i, j) = (1 + \phi h_{ij}) e^{-\phi h_{ij}},$$

where $h_{ij} = |s_i - s_j|$, and ϕ is indicative of the correlation range (Matérn, 2013). Capturing the correct spatial correlation distance is particularly important. Formulating an accurate surrogate GP model depends on getting this parameter as correct as possible. One could also add anisotropy in this kernel, with correlations depending on north–east directions between locations, and the methodology presented next would still work. However, based on the ocean model data, there was no significant anisotropy in the current case.

A standard tool for estimating correlation range is the *variogram*. Given spatially dependent data, the variogram can estimate the degree of spatial correlation as a function of distance (Cressie & Wikle, 2011). The same hindcast temperature data from SINMOD was used to find ϕ using this procedure, as shown in Figure 6. The derived variogram is fitted from the residuals after the trend in the input data has been subtracted, under the assumption of smooth, slow-changing, spatial variance terms—this is necessary to obtain a correct evaluation of the

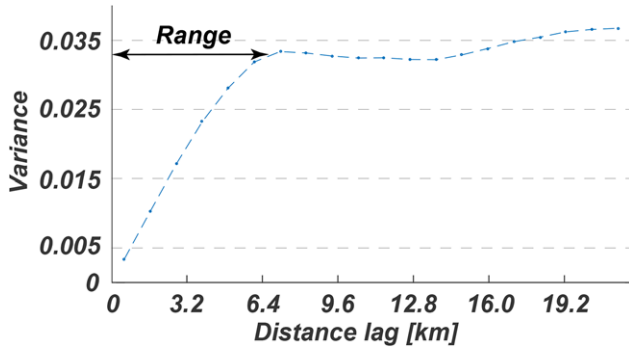


FIGURE 6 The final variogram from analyzing SINMOD temperature data

underlying variability. As the distances increase along the x-axis, the spatial dependence decreases, increasing the variogram, until a limit is reached (horizontal black line on y-axis in Figure 6). At this limit, the points no longer yield any correlation based on data values, and it is therefore possible to provide the lag distance/range for the correlation at around 5–7 km. The parameter estimates could be improved using maximum likelihood estimation based on the density function in Equation 1 for the ocean model data, see e.g., Stein, Chi, and Welty (2004).

The GP we use, therefore, has a nonstationary kernel function and a bias correcting mean function, based on temperature data from SINMOD. Exploratory data analysis shows residual plots that are approximately Gaussian, justifying using a GP for temperature data in the current setting. The process x is assumed to be relatively constant over the data gathering period. To account for minor time variations, we add process noise Q_t , that is accumulated over the survey period, to capture minor variability from sea currents (current velocity is typically 0.2 m/s on average (Figure 3), while vehicle speed over ground is about 1.5 m/s), see Equation 5.

4.2 | Data assimilation

Measurements are acquired sequentially for time steps $1, \dots, T_f$, where T_f is typically mission duration. Only measurements from a specific depth layer (70–90 m) are used for assimilation, to focus on the dynamics related to the characteristics of the Froan archipelago (see Section 3.4 and Figure 5 for further details).

A sampling design is defined by d_1, \dots, d_{T_f} , where d_t is a survey location at time t . The successive survey design until time t is denoted by $d_t = (d_1, \dots, d_t)$. The measurement model for design d_t at time t is given by

$$y_{t,d_t} = G_{t,d_t} x + v_t, \quad (4)$$

where y_{t,d_t} is a $m_{t,d_t} \times 1$ vector of observations along a survey line, and the matrix G_{t,d_t} of size $m_{t,d_t} \times n$ contains “1” entries only at the designated d_t indices, and 0 otherwise. The error term $v_t \sim N(0, R_{t,d_t})$ is measurement noise. The covariance matrix R_{t,d_t} is typically set to a constant matrix with only diagonal elements (Wunsch & Heimbach, 2007), and there is no dependence of measurement error terms over time.

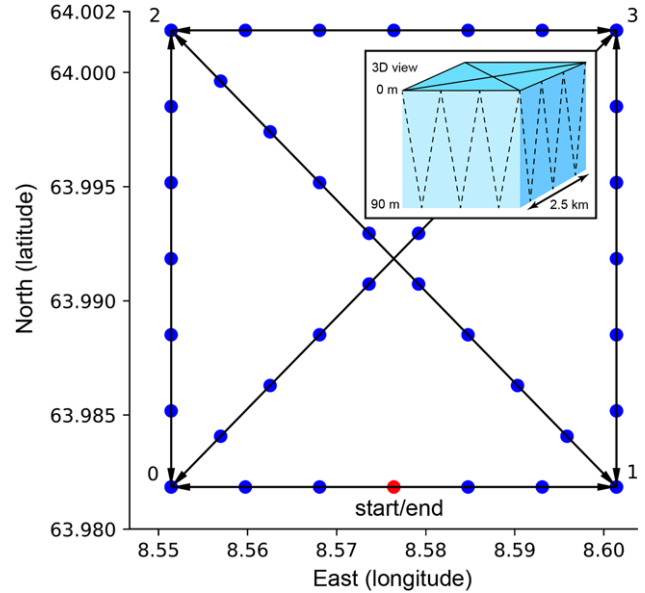


FIGURE 7 The waypoint graph G used in experiments in the Froan region, with the depth range 0–90 m. Because the AUV is undulating, the graph takes 4 hr to survey, visiting five nodes

Under Gaussian linear modeling assumptions, the sequential updating of data leads to the Gaussian distribution $p(x|y_{1,d_1}, \dots, y_{t,d_t})$. The common Gaussian equations for conditioning give the updated mean $m_{t,d_t} = E(x|y_{1,d_1}, \dots, y_{t,d_t})$ and variance $P_{t,d_t} = \text{Var}(x|y_{1,d_1}, \dots, y_{t,d_t})$ at every stage. These equations are recursive over the data gathering steps:

$$\begin{aligned} \bar{P}_{t,d_t} &= P_{t-1,d_{t-1}} + Q_t I(t = t_{wp}), \\ S_{t,d_t} &= G_{t,d_t} \bar{P}_{t,d_t} G_{t,d_t}^t + R_{t,d_t}, \\ K_{t,d_t} &= \bar{P}_{t,d_t} G_{t,d_t}^t S_{t,d_t}^{-1}, \\ m_{t,d_t} &= m_{t-1,d_{t-1}} + K_{t,d_t} (y_{t,d_t} - G_{t,d_t} m_{t-1,d_{t-1}}), \\ P_{t,d_t} &= \bar{P}_{t,d_t} - K_{t,d_t} G_{t,d_t} \bar{P}_{t,d_t}. \end{aligned} \quad (5)$$

The first equation above, contains the step where the accumulated process noise Q_t is added, when reaching the waypoint goal (finishing a survey line) and activated by the indicator function $I(t = t_{wp})$, where t_{wp} indicates the arrival time at a waypoint goal.

4.3 | Waypoint graph

The different paths for an AUV are encapsulated in a waypoint graph $G = (V, E, D)$ with four corner nodes $v \in V$, $v = \{0, 1, 2, 3\}$ and edges between the nodes given as $e \in E$, $e = \{(0, 1), (0, 2), (0, 3), (1, 0), (1, 2), \dots, (3, 2)\}$, represented as arrows, as shown in Figure 7. Each edge $e_j, j = 1, \dots, n_e$, where n_e is the number of edges in e , is referred to as a *survey line* or graph edge. These lines also contain a set of *sample points* (the dots on the lines in Figure 7) collected for each survey line e_j in the vector $d_j \in D$, $d_j = \{D|e_j\}$, where D is the set containing all the sample points in the graph. As

noted, variability in the water column tends to be greater along the vertical dimension—to appropriately measure this variation, the AUV undulates (with a fixed angle) up and down, in what is known as a “yo-yo” pattern throughout the mission. The sample points (used to evaluate the objective function) are spaced out according to the depth, angle of the yoyo, and the distance of the survey line, having twice the number of sampling points as the number of crossings of the given depth layer. For the configuration used here, this results in a sample point spacing of 416 m. Measuring the entire water column is important (rather than only undulate between the 70 and 90 m depth band), as both surface phenomena (i.e., SST, surface warming effects, chlorophyll, etc.) and deeper processes (influx of AW) are of interest. The AUV then traverses the graph going from one node to another: for example, going from node 1 → node 2, along the survey line $e_5 = (1, 2)$, contains the sample points d_5 .

4.4 | The objective function

The aim of an objective function is to evaluate and prioritize the different survey alternatives (graph edges), accounting for prior (model) and in situ information. Focusing solely on reducing uncertainty in the ocean model, one solution would be to bias locations yielding the largest reduction in variance, or to use mutual information (Krause et al., 2006), to determine the graph edge having the largest information gain (highest entropy reduction). However, neither of these criteria are capable of readily using incoming measurement data y_{t,d_t} , consequently making the strategy deterministic (Eidsvik, Mukerji, & Bhattacharjya, 2015). Given the large uncertainty in oceanographic sampling, the informative value of in situ measurements cannot be overlooked. Still, the conundrum of exploration versus exploitation continues to persist, and finding a functional balance is necessary.

The GP representation is well suited for this purpose because it holds prior information about the temperature variance (uncertainty), in addition to assimilating the incoming measurements into the mean parameter.

For achieving effective adaptability, the upper ocean temperature variability and trends derived from the GP are used to guide the data collection process through variance and gradient measures. Temperature is a prominent factor in the Froan region, because measurements associated with CW and FW are different from AW (Sætre, 2007), with a well-defined front between the cold and low-salinity NCC and the warm and dense AW (Ikeda, Johannessen, Lygre, & Sandven, 1989). These temperature-laden fronts are found all year; horizontal gradients of 0.5°C/km can be observed, depending on the season (Sætre, 1999) and increased variability and levels of primary productivity is expected in areas where these water masses meet. Faced with high model uncertainty, variance is preferred over entropy as the metric for uncertainty in our approach, because of its simpler form and wider acceptance as a measure of spread in a numerical model (Baafi & Schofield, 1997).

The objective function is formulated as a balance between gradient intensity and reduction of variance—the rationale being that in cases with uniform temperature conditions, the strategy would prioritize navigating according to the variance. Or in the opposite case, if a

thermal gradient is discovered, using the gradient as a means to steer toward locations indicative of these changes, directing the AUV toward nonuniform conditions. The objective function is evaluated using the surrogate GP model formulated in the preceding sections. The objective function is evaluated on the sample points k_j related to each alternative survey line d_j given as

$$f(d_j) = \operatorname{argmin}_{d_j} \left\{ \frac{\omega_p}{n} \operatorname{trace}(\mathbf{P}_{t,d_j}) - \frac{\omega_g}{n_k} \sum_{k_j=1}^{n_k} \nabla g_{t,k_j} \right\}. \quad (6)$$

The first term expresses variability at all locations, with n being the total number of locations. The second term provides the weighted gradient summed over the sample points k_j , where the number of points along the line is n_k . Both terms are normalized prior to subtraction, in order to allow reconciliation between the variance and gradient term. The influence between the variance and gradient can be adjusted using the weights ω_p and ω_g . For simplicity, we have set the weights to 1; depending on the application, these may be adjusted. The gradient is calculated for the mean value at the survey points, weighted by their uncertainty as

$$g_{t,k_j} = \frac{m_{t,d_j}(k_j)}{\mathbf{P}_{t,d_j}(k_j, k_j)},$$

where m_{t,d_j} and \mathbf{P}_{t,d_j} are terms from Equation 5. Before calculating the scaled gradient, the term \mathbf{P}_{t,d_j} is normalized using the global minimum as follows ($\min_{k_j} [\mathbf{P}_{t,d_t}(k_j, k_j)] / \mathbf{P}_{t,d_j}(k_j, k_j)$) and has a lower limit to avoid over emphasis on already visited locations. The best node to visit will be the node with the connecting survey line yielding the lowest objective value. Explorative survey lines would reduce diagonal elements of \mathbf{P}_{t,d_j} more than the lines previously surveyed. And finally, ∇ in Equation 6 is the operator using second order central differences to compute the actual gradient value.

Note that several other criteria are possible. Entropy measures or average variance reduction are commonly used, but for GP these will not depend on the data (Eidsvik et al., 2015). The criterion in Equation 6, which includes the temperature gradients, allows adaptive sampling where the survey paths can depend on the realized data. In simulations we also ran tests with a criterion aiming to classify significantly large temperature gradients in the main current direction, that is, $E[\nabla_{\theta} x_t | \cdot] - \sqrt{\operatorname{Var}[\nabla_{\theta} x_t | \cdot]}$, where the conditioning represents currently available data, and θ is a predefined direction. One could also go further to account for the uncertainty in future data along the next sample line that entails an integral over the data (Bhattacharjya, Eidsvik, & Mukerji, 2013; Eidsvik, Martinelli, & Bhattacharjya, 2018), or even use the expectation over future lines, with additional computational complexity for nonmyopic approaches. But the simple weighting in Equation 6 is a practical solution which gave reasonable results for our field tests, and we leave more complex objective functions for future work.

Because the path of the AUV only considers one node into the future, the approach is a greedy/best-first search. Using such a myopic approach, with a one node horizon, is assumed to be sufficient as the ocean model skill is typically low, resulting in substantial uncertainty when executing the sensing strategy. Additionally, due to control,

actuation, and navigational errors in part due to ocean currents, the position of the AUV will deviate from the optimal route—more details are given in Section 6. Note that the information utility used here is a single objective function with only one solution. Extension into multiobjective functions would be possible to account for other environmental or operational parameters such as energy, safety zones, and operation of other vehicles; or more decision analytic criteria related to algal bloom treatment, fishing policies, and dynamic placement of fish farms.

4.5 | The GASA algorithm

The GP model, objective function, and the waypoint graph G are then collected in an algorithm, which is to run onboard during execution. Using the different survey alternatives the algorithm iterates through possible survey lines and calculates their objective value, utilizing the variance and mean estimates from the GP model. The details of these steps are given in the greedy adaptive sampling algorithm (GASA) in Algorithm 1.

ALGORITHM 1 The GASA algorithm.

```

1 Initialize GP, Graph:  $G$ 
2 update_GP_bias() %Runs only once
3 while active do
4   if goal is reached then
5     for survey line in G do
6       Evaluate objective function (Eqn. (6)).
7     end
8     Find the best survey line.
9     Set the corresponding node as the goal.
10    Add dynamic uncertainty component in spatial GP model.
11  else
12    Continue towards goal.
13    Collect data.
14    Update model (Eqn. (5)).
15  end
16 end

```

In an operational scenario, once the AUV is deployed, it will need to travel to the starting point of the survey graph, before initiation of the algorithm, having time to update the bias for the prior mean on its way. To avoid overfitting, the bias correction will only occur if the observed model discrepancy is above $\pm 1^\circ\text{C}$. Once the starting point is reached, the algorithm activates and begins evaluating the alternative survey lines available at its current location. Once the objective values have been calculated, the best survey line and the corresponding node is set as a waypoint goal for the AUV to visit.

4.6 | Implementation

Prior to the deployment, the GASA algorithm was tested in a simulated environment, identical to the embedded system in the AUV. The setup consists of three essential components; a virtual ocean simulator, an AUV vehicle simulator and an autonomous agent architecture (Figure 8).

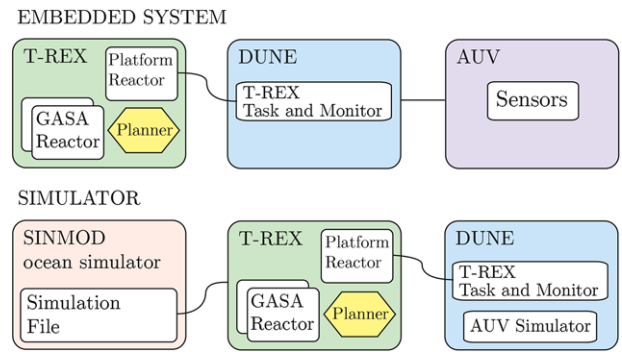


FIGURE 8 A block diagram layout comparing the embedded and simulated systems used

An interface that directly couples the SINMOD model provides 3D ocean data that are used to simulate sensor readings, reproducing actual ocean conditions at a given time, depth, and location. The Unified Navigation Environment in DUNE (Pinto et al., 2012), handles the

AUV simulation, and is used for navigation, control, vehicle supervision, communication, and interaction with actuators—DUNE is running onboard the AUV as well. On top of the hierarchy sits the autonomous agent architecture T-REX (Teleo-Reactive EXecutive), which synthesizes plans and uses an artificial intelligence based automated planning/execution temporal framework to execute tasks continuously, as sensing and control data are fed to it. Details of T-REX are beyond the scope of this work; readers are encouraged to refer to Py, Rajan, and McGann (2010), Rajan and Py (2012), and Rajan, Py, and Berreiro (2012). The communication between DUNE and T-REX is handled by the LSTS toolchain (Pinto et al., 2013)[¶], which provides the back-seat driver API to DUNE allowing external controllers, such as T-REX, to provide desired poses for the platform while receiving progress updates on their attainability.

[¶] <http://lsts.pt/toolchain>.

TABLE 1 Results from running 1,000 mission simulations

Run	Mean criteria score ^a	RMSE ^b
Random route	+0.15	0.61
GASA: both variance and gradient	-0.21	0.36
Only variance (gradient kept constant -0.33)	-0.06	0.37
Only gradient (variance kept constant +0.33)	-0.15	0.49

Note. RMSE = root mean square error.

^aThe mean score from the objective function for each chosen alternative.

^bThe root mean square estimation error between the underlying temperature field and the estimated Gaussian process (GP) temperature field.

GASA and dependencies were implemented as *reactors* that are internal control loops in the T-REX framework capable of producing goals that the planner integrates in a series of actions (e.g., Goto, Arrive_at ...), which are finally collected to form a plan. This plan is then distributed through the framework and checked for errors such as operational limitations, before dispatch to DUNE, which handles low level control and execution. The mission is hence continuously monitored by T-REX, as it follows the *Sense* → *Plan* → *Act* control methodology.

4.7 | Simulation

We conducted an empirical study comparing the GASA algorithm and preplanned randomly generated routes to assess performance, along with simulations using SINMOD nowcast data to provide further insight into the resulting behavior, using the same GP parameters, graph, and objective function as in the at-sea experiments. The following procedure was used for the empirical simulations:




1. Generate a random GP temperature field.
2. Simulate 1,000 different missions visiting five nodes using GASA with randomly chosen routes.
3. Collect the criteria score and the final root mean square error (RMSE).

The drawn temperature fields had a variation 1.5°C. If larger temperature differences are expected, one should evaluate to reduce the influence of the gradient term.

As shown in Table 1, the random route has a high criteria score and a high RMSE; this was to be expected. Using only variance results in a lower RMSE as it will seek to explore rather than exploit. In contrast, using only the gradient will put emphasis on exploitation, yielding higher RMSE results. When using both terms, the resulting behavior is a balance.

In addition, various simulations were conducted using both hindcast, and forecast (nowcast) data from the Froan area. However, for the sake of clarity, analysis of simulations using nowcast data from May 4, 2017 is presented, where the example illustrates the interplay and influence of the variance and gradient components. To demonstrate this, three simulations were carried out with the objective function

TABLE 2 Simulated routes using different terms in the objective function

Run	Route (nodes)	Remarks	Visual path
Simulation 1: variance	2, 3, 0, 2, 1	Variance only	
Simulation 2: gradient	3, 2, 0, 1, 2	Gradient only	
Simulation 3: both	2, 3, 0, 2, 3	Variance and gradient	

considering: only variance, only gradient, and finally both (shown as Simulations 1–3 in Table 2). The simulation considers a route of five consecutive nodes to be visited in a prioritized fashion depending on their objective value.

The underlying nowcast covers the sea state for May 4, 2017. Because the algorithm only updates using measurements from the 70 to- 90 m depth interval, the temperature is expected to be relatively homogeneous, except in areas with the influx of AW. Two clear trends are visible in the prior variance (Figure 9a) and mean (Figure 9c). Both variance and temperature gradients are higher toward the north, suggesting that the AUV should start by mapping here first. The prior variance and mean, both derived from May 2016 hindcast data, were kept constant, both during simulation and during field deployments.

Using only the variance (Simulation 1) for navigation, results in a maximum reduction of the prior uncertainty and the nodes: 2, 3, 0, 2, 1, thus prioritizing the high-variance hot spots close to nodes 2 and 3. Using only the gradient (Simulation 2) leads to a route favoring the survey lines with the greatest temperature change. The gradient follows the outer edges of the graph, visiting the north region first following the nodes: 3, 2, 0, 1, 2. Because the gradient depends on the collected temperature measurements from the nowcast, the gradient is using in situ information to change its path, in contrast to the variance, having a predetermined track based only on prior knowledge.

Combining both influence from variance and gradient in Simulation 3 shows the interplay between the two information measures. The executed path, visible as Simulation 3 in Table 2 and Figure 9b, shows priority of exploring the north-south axis. As the gradients are weighted by the prediction accuracy, the initial path choices are dominated by variance because the gradients will have high uncertainty. Then, as measurements reduce the uncertainty of the mean estimation, the gradient effect becomes more influential. Still, because the temperature distribution is relatively homogeneous for this example, the gradients are approximately the same for each alternative, resulting in a dominance of variance right until the end where the gradient changes the choice to node 3. As the model only updates if measurements are within 70 to- 90 m depth, the estimated fields in Figure 9b and d are uneven, leaving only parts of the grid updated, because the AUV is traveling in a yo-yo pattern. In addition, the covariance range is limited and locally changing as a result of the covariance modification in Equation 3, allowing the information to be “spread” nonuniformly, hence the uneven spots in Figure 9b. Differences in paths for various mean, variance, and correlation models were also studied prior to deployment.

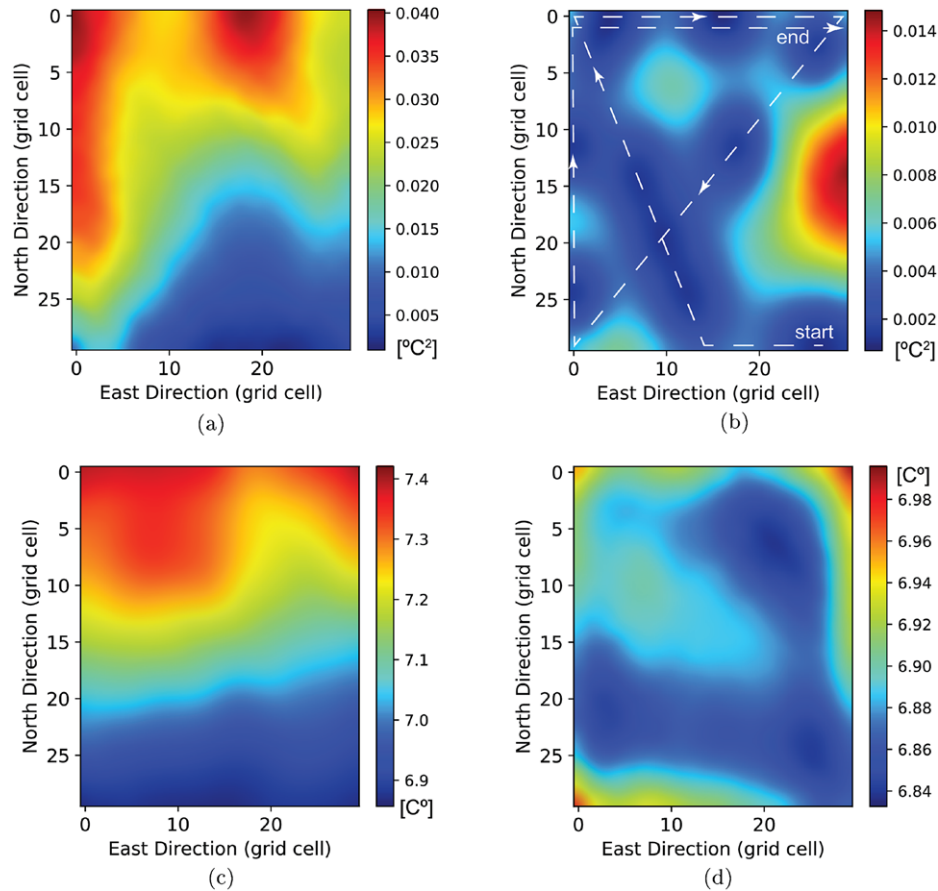


FIGURE 9 Simulation prior to deployment using both terms in the objective function with nowcast data from May 4th, 2017 at ~10 a.m. Temperature variance for operational area *at start*. Note the location of the highest variance. (b) The final estimated variance and the traveled path *at end*. Note the spots of low variance. (c) The estimated temperature at the survey area *prior to deployment*. (d) The final GP regression of the temperature field *at end*

For a discussion on GP sensitivity to variance and correlation parameters for sequential sampling schemes, see Eidsvik et al. (2018). Note that the dynamic nature of the processes studied here would be highly nonlinear and non-Gaussian over a longer spatial and temporal range, and in the future one can imagine having more complex spatiotemporal proxy models on-board the AUV itself.

5 | FIELD EXPERIMENTS

The experiments at sea aimed to verify our algorithm's ability to adapt mission execution based on in situ measurements, and demonstrate its capability to spatially prioritize data collection, using ocean model driven predictions encapsulated in a stochastic model. They were carried out between the May 4 and 12, 2017, using the operational area and waypoint graph shown in Figures 7 and 10 of the Froan archipelago.

Inclement weather on the Norwegian west coast led to numerous postponed deployments, but two full missions, referred to as Surveys 1 and 2, were conducted during this period. Both surveys used the same prior data (variance and mean from Figure 9). Doing so was important for demonstrating adaptability toward the environmental conditions while keeping the initial conditions the same for both surveys.

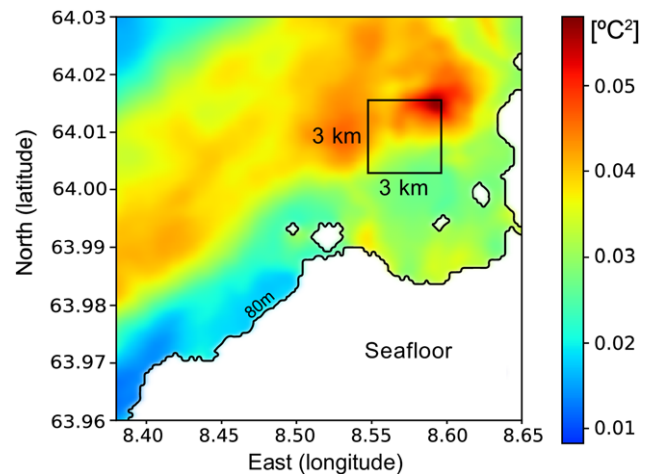


FIGURE 10 The distribution of temperature variance across the Froan coastal region with the operational area indicated; note the 80-m isobath

5.1 | Experimental setup

Our scientific focus was the upper water-column and the effect of physical forcings on phytoplankton dynamics of the Froan coastal region, which we targeted using temperature variability. Consequently,



FIGURE 11 NTNU's light AUV platform (*Harald*) for upper water-column exploration used in our work—the CTD is visible in the nose. The AUV has an excess of 24 hr in-water operational capacity with a range of sensors in addition to the CTD

before bringing the system to the field, an approach similar to Sakov and Oke (2008) was used to identify an operational area where shifts in temperature would be prominent and hence interesting from both a model and oceanographic perspective. The input data to this analysis were hindcast realizations from SINMOD (May 2016), reflecting the changing temperature distribution at 80-m depth using a planned deployment time between 8:00 a.m. and 2:00 p.m., where the empirical variance was estimated by applying Equation 3 and shown in Figure 10.

The survey area was confined to the eastern region close to the point of highest empirical variance, but also sufficiently near the shallower waters in the event an emergency recovery of the AUV and/or dealing with unfavorable weather conditions. To operate safely the waypoint graph G (Figure 7) was limited within the operational area $3 \times 3 \text{ km}^2$ to $2.5 \times 2.5 \text{ km}^2$ (allowing a 500-m drift margin), permitting a reduced search area and enabling the AUV to be monitored using acoustics from a vessel stationed at the center of the survey pattern. Although the experiments were constrained by this one graph for these pilot deployments, the framework is general and can be extended to a series of connected graphs of any shape. In addition, having a greedy (one-step look ahead) planner as well as a simple waypoint graph allowed us to work with a constant and reliable computational load on the AUVs CPU, while maintaining communication to the vehicle in the harsh conditions offshore.

Our robotic platform consisted of a light AUV (Sousa et al., 2012) equipped with a 16 Hz Seabird “Fastcat 49” active conductivity, temperature, and depth (CTD) sensor providing temperature and salinity measurements, see Figure 11. The CTD is active as it continuously pumps water, ensuring that a fresh sample is observed. The accuracy of the CTD instrument is $\pm 0.0003 \text{ S/m}$ (conductivity), $\pm 0.002^\circ\text{C}$ (temperature). The AUV was also equipped with a Wetlabs EcoPuck for chlorophyll a concentration, color dissolved organic matter (cDOM) and total suspended matter (TSM). The embedded system in Figure 8 hosting the GASA framework was operating on a multicore GPU NVIDIA Jetson TX1 single board computer, specifically developed for autonomous systems. With a lithium polymer battery bank, the AUV had an operational capacity in the water column exceeding 24 hr of continuous operation.

TABLE 3 Executed routes and deployment times, May 2017

Run	Route (nodes)	Deployment time
Survey 1—May 9	2, 3, 0, 1, 3	10:02 a.m.
Survey 2—May 12	2, 1, 3, 0, 2	10:15 a.m.

Each survey took 4 hr to complete, with five nodes to visit during this period. Restricting the adaptation to only five choices, and within the waypoint graph, was necessary to manage deployment and recovery within limited weather windows. Because full coverage of the region could be attained with the AUV, we emphasize that the results from the field operations should be seen as applicable to cases in which intensive sampling is not feasible.

The GP model used a grid resolution of 30×30 on a $2.5 \times 2.5 \text{ km}^2$ region ($83 \times 83 \text{ m}^2$). The GP model was configured with a prior mean and variance (seen in Figure 9) associated with the temperature distribution at 70 to 90 m depth. Updating these priors was limited to measurements collected from this depth. Limiting the information used by the objective function to these depths was to specifically target the temperature dynamics induced from warmer AW, as discussed in Section 3.4.

5.2 | Results and evaluation

This section first presents the AUV data and the details related to the GASA algorithm, followed by a comparison to SINMOD model forecasts (nowcasts) and data from remote sensing, buoy, and ship-based measurements.

Figure 12 shows recorded temperature versus depth taken along the transect for the two surveys, along with the maps of the executed survey path superimposed on the SINMOD model predictions for both deployment days. The survey paths from the maps are collected and shown in Table 3, along with the deployment time and date. The objective values used to differentiate the route choices is presented in Figure 13.

We observe that two different strategies have been executed, underpinned by the GP priors and the assimilated temperature measurements. As the GP priors are the same, the observed difference between the paths are provided by separate temperature conditions. This is apparent in Figure 12a and c, with Survey 2 clearly having a more shallow prominence of warmer AW, depicting the thermocline (dashed lines) shifting from 65 to 40 m, the same shift predicted by SINMOD in Figure 5. The deep salinity measurements come close to 35.0, suggesting the water is of Atlantic origin, which is distinctly more saline than FW (≤ 32) and CW ($32 \leq 35$). This is also confirmed from the CTD measurements taken from the R/V *Gunnerus* shown in Figure 17. There is also a visible difference in surface warming, which is traceable in both buoy and remote sensing data.

Evaluating the adaptive behavior, as in simulation, node 2 is always taken as the first node to visit. This is expected as the prior data are identical at this point, and no measurements are assimilated; objective values for the first node choice in Figure 13a and b confirm this. After reaching node 2, the recorded data come into consideration because exposure to the warm water influx is different, each survey will have a

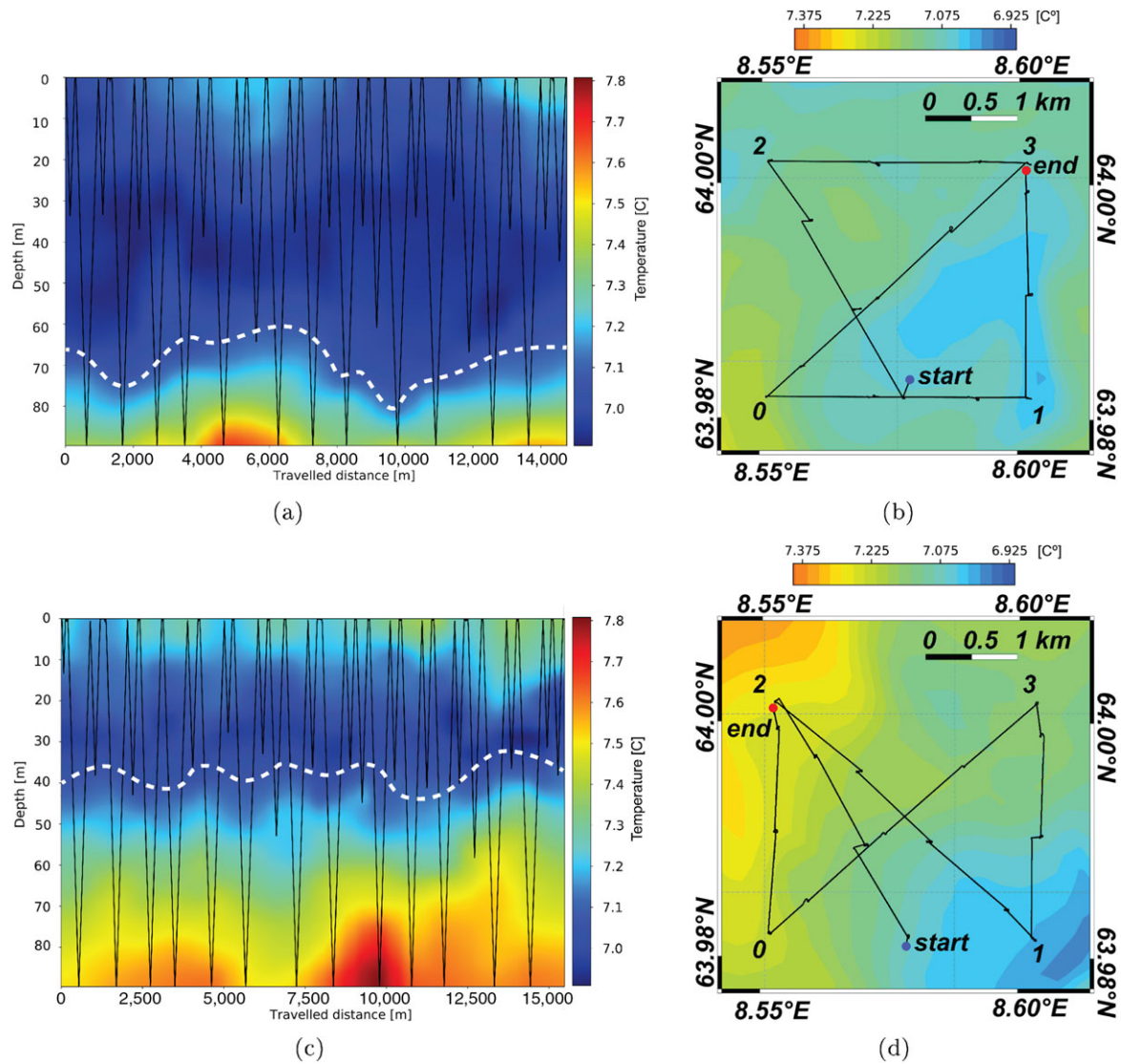


FIGURE 12 Results from the AUV survey on the May 9th (Survey 1) and May 12th, 2017 (Survey 2). Yo-yo pattern (black line) and the temperature distribution for Survey 1. (b) Map of the executed path for Survey 1, SINMOD realization for May 9th in background. (c) Yo-yo pattern and temperature for Survey 2. (d) Executed path for Survey 2, SINMOD realization for May 12th in background. In (a) and (c), temperature distribution in the survey area and thermocline (white lines) influenced by AW (temperatures are interpolated to cover the plot surface) is shown. In (b) and (d), the path generated by the GASA algorithm for the two surveys is shown. The gaps in the position on the plots are surfacing events to correct for drift and navigational errors in the water column

distinctive posterior mean temperature field and hence gradient influence. Consequently, the intensity and direction of the gradient will also be different. After reaching node 2, the first decision with posterior information is made. This choice is the most intuitive to consider and interpret, as only the data along the first survey line are assimilated into the onboard GP model. Evaluated from node 2, a transect toward node 3 would be most beneficial for reducing the variance (comparing with simulations in Table 2), if no strong temperature trends are to be observed. This is the case for Survey 1, which tracks to node 3, after node 2. More interestingly, Survey 2 tracks back toward node 1. Clearly, this is not optimal for reducing the variance as several measurement locations will be close to the first survey line. One can therefore argue that this choice is dominated by the influence from the recorded temperature data, which is visible as a difference in score at the second evaluation step in Figure 13b.

Additionally, because the uncertainty is low around the first transect, this gradient is weighted higher compared to other gradients with larger uncertainty. After reaching node 1, the AUV in Survey 2, tracks toward following the paths associated with Survey 1, visiting nodes 3 and 0, which suggests that the influence of variance is dominant. As observed in Figure 12b and d, Survey 2 has a hourglass pattern, while Survey 1 has a more mixed survey pattern. These characteristics will be compared to the model and external data in the following sections.

5.3 | Model correspondence with AUV data

Deviation between recorded data and the simulated predictions is to be expected. Considering assimilation back to the model, the question is as follows: Can the observed discrepancies contain contextual information that can augment the model and enhance ocean prediction?

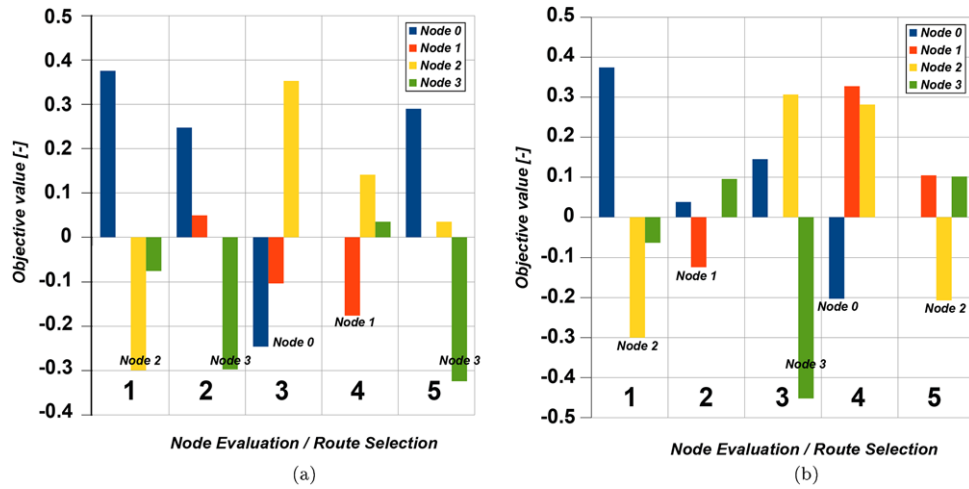


FIGURE 13 Values for the objective/utility function used to evaluate the different survey alternatives (negative score is preferred). (a) Survey 1 and (b) Survey 2. The choices correspond to the executed paths in Table 3

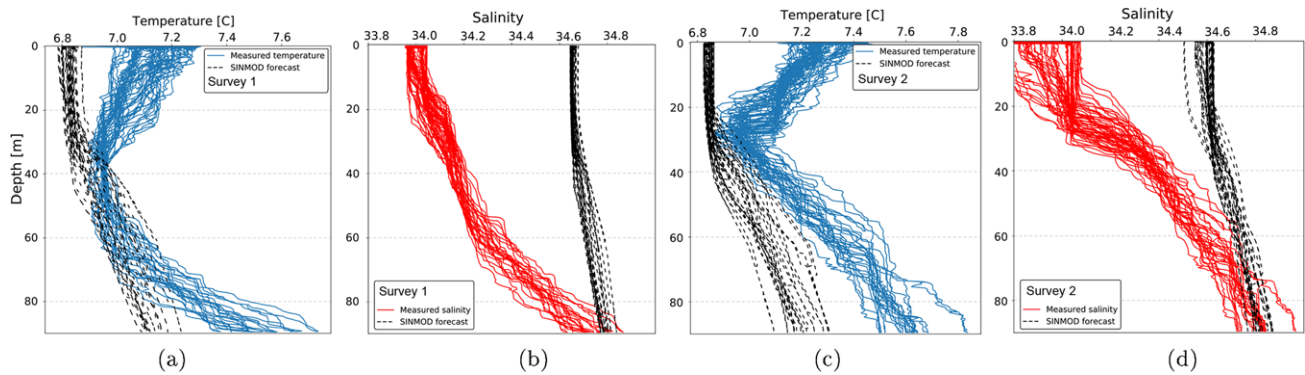


FIGURE 14 Vertical comparison of AUV measurements with SINMOD nowcast data. (a) Temperatures for Survey 1. (b) Salinity for Survey 1. (c) Temperatures for Survey 2. (d) Salinity for Survey 2

Although a full diagnosis of the model accuracy is not within the scope of this work, a general overview and direct comparisons are shown on which to base further analysis. Because undue reliance on one data source increases the risk of erroneous comparisons, consequently in this section we compare SINMOD data and AUV observations, followed by Section 5.4, where we provide supporting data from ship, buoy, and remote sensing from the same spatiotemporal domain.

During the field experiment period SINMOD provided nowcasts (48-hr forecasts) used to cross-validate the in situ measurements and study the experienced behavior. Comparing the executed paths to the 80-m SINMOD nowcasts (shown in the background in Figure 12b and d) suggests that Survey 2 accounts for a temperature trend that is warming toward west, crossing the gradients in a manner one would expect. More uniform conditions are predicted for Survey 1, which results in a more variance dominated survey.

Figure 14 presents temperature and salinity measurements from the AUV with the SINMOD nowcasts superimposed (dashed lines). The immediate impression is that the model shows a tendency to *underestimate* the surface warming present in the AUV data; a bias in salinity is also present. The correspondence is good in the 70 to 90 m depth in which the GP data assimilation and GASA algorithm were active.

The temperature difference is easier to study using Figure 15, presenting the temperature deviation spatially within the survey area (birds-eye view). Figure 15a and b makes it possible to study, where in the survey area, the temperature deviation between the nowcasts and reality was the highest. The northeastern corner of the model was the weakest in terms of predicting ocean temperature, for both surveys, being warmer than expected. This may explain why GASA in both cases chose to cross over from node 3 to node 0. The deviation between the measurements and the nowcast is not influencing the AUV behavior directly because the objective function only evaluates the balance between variance and gradient. However, if the number of nodes to visit is higher (e.g., more than 5), we would expect this region to be revisited as the objective value would favor the temperature gradient. Indirectly, this would result in a higher sampling density where model discrepancy would potentially be high, as a result of this gradient. The region corresponds to the maximum-variance hot spot (Figure 10), which suggests a connection between temperature variation and model uncertainty, important for validating our approach in developing the objective function.

Figures 14 and 15 can be used to give the first impression of the discrepancies, but cannot be used as the proof of model error, as a range of sources may contribute to the mismatch, including

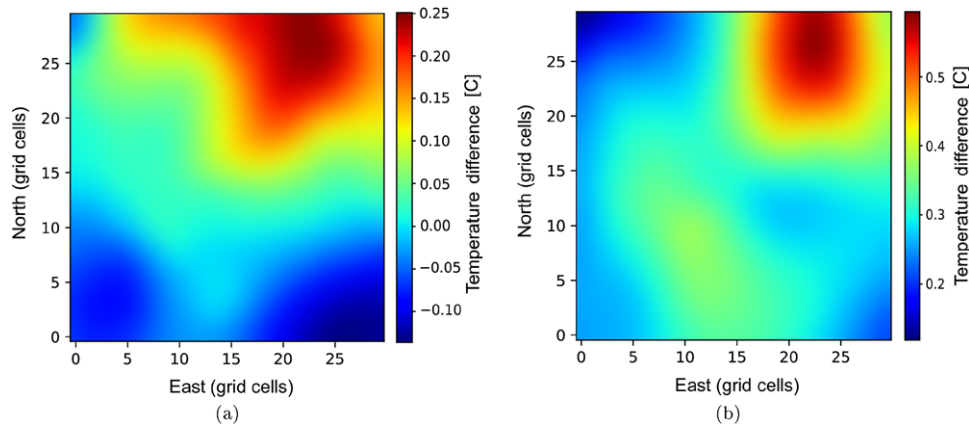


FIGURE 15 Subparts (a) and (b) show the spatial comparison of predicted SINMOD nowcast and the estimated GP temperature field (survey area seen from above at 80 m depth). (a) Temperature discrepancy Survey 1. (b) Temperature discrepancy Survey 2

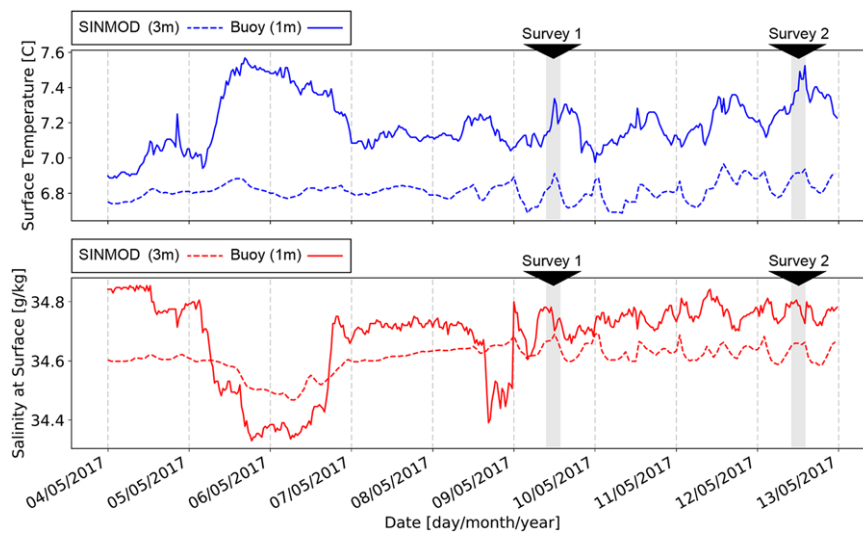


FIGURE 16 Results from a moored buoy, from May 4 to 11, 2017. Temperature and salinity measurements from the buoy at 1 m depth during the operational period, overlaid on SINMOD predictions at 3 m depth; Surveys 1 and 2 are indicated in grey

errors in initial conditions. The results nevertheless demonstrate how adaptive and data-driven approaches can improve ocean modeling, by revising a priori uncertainty assumptions and providing information that can greatly focus analysis of model shortcomings and inaccuracies.

5.4 | Buoy, ship-based, and remote sensing data

To get a full picture of the environment and ground truth the SINMOD and AUV data, supporting data sets from the other marine platforms are presented in this section. The measurements from a moored buoy in Figure 16 show the long-term fluctuation in the area. The buoy is located further inshore, 3 km from the AUV survey area; see Figure 19b.

The buoy data show a trend of sun-driven surface warming during the AUV deployments, with Survey 2 having a higher peak temperature during the deployment corresponding to sea SST products from remote sensing. The SINMOD nowcast prediction at the buoy location, shown with the dashed line, follows the trends well albeit with some

bias, although certain events such as the salinity drop before May 9, 2017, is not picked up by the model.

The results from Surveys 1 and 2 indicate a significant difference in the influence from AW, visible in the thermocline line in Figure 12a and d. Comparing these results with CTD measurements made from the R/V *Gunnerus* in Figure 17 and the SINMOD prediction in Figure 5, the same thermocline dynamics can be found. Most notably for the outermost stations (2 and 6), both taken at high tide, there is a large shift in both temperature and salinity between May 9 and 10, 2017.

A significant difference in chlorophyll *a* concentration (Figure 18) for the two deployments is captured in the remote sensing data. Due to cloud cover, the retrieved data area is patchy; despite this, there is clearly more chlorophyll *a* concentrated in the surface during Survey 1, in agreement with the in situ chlorophyll measurements from the AUV and the R/V *Gunnerus*.

It is important to stress that the peak chlorophyll concentration at 15 to 20 m depth cannot be detected from space and that sparse coverage from ship-based sampling can be augmented with AUV data to render a more precise in-depth picture of chlorophyll

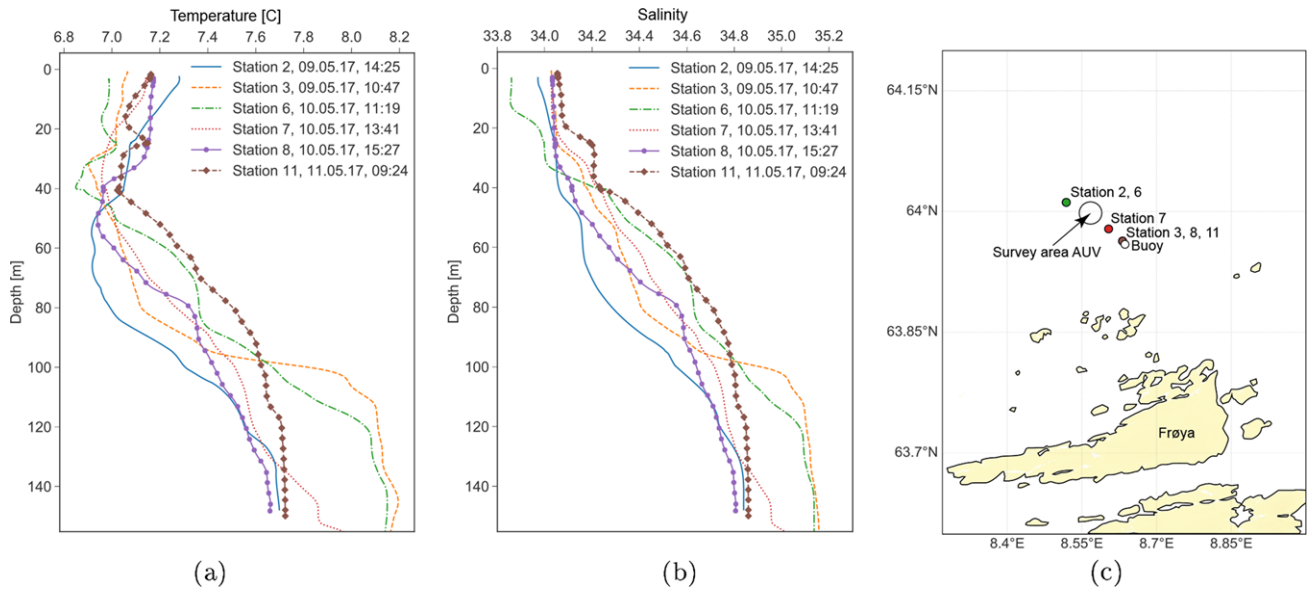


FIGURE 17 Results from the R/V *Gunnerus* operations from May 9 to 11, 2017 (a) Temperature profiles. (b) Salinity profiles. (c) CTD cast locations. Vertical profiles from CTD measurements made by *Gunnerus* with temperature variability showing the influx of AW moving up and down in the water column

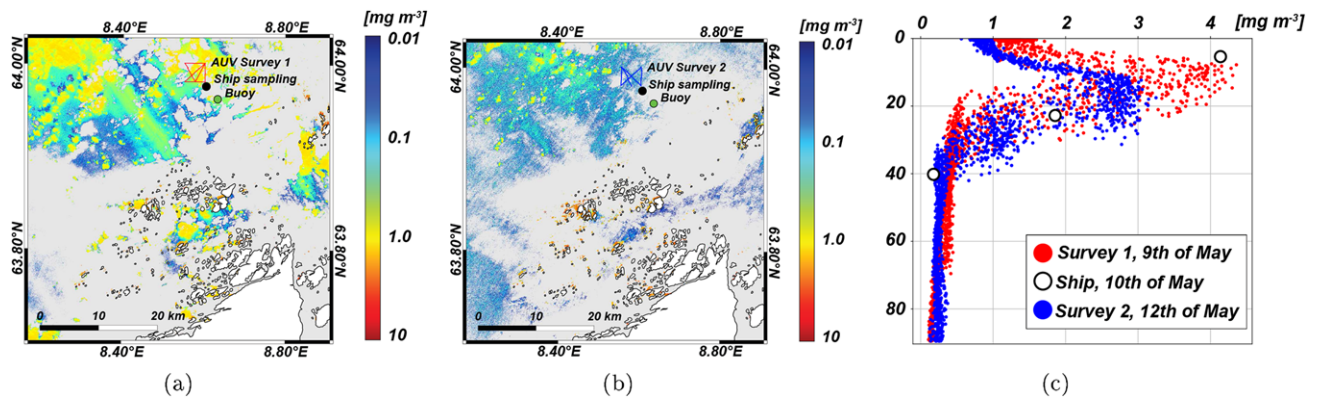


FIGURE 18 Chlorophyll *a* concentration for May 9 and 12, 2017, processed from Copernicus Sentinel Data (Sentinel-2A) OC2 (Vanhellemont & Ruddick, 2016) compared with in situ measurements from AUV and the research vessel (a) Sentinel-2A, CHL OC2, May 9, 2017, 10:56 a.m. (b) Sentinel-2A, CHL OC2, May 12, 2017, 11:13 a.m. (c) AUV and vessel R/V *Gunnerus*, May 9, 2017

structure. This demonstrates why we need to combine information from several sources to arrive at a deeper understanding of ongoing processes.

Comparing across the different measurement platforms, Figure 19 shows the nowcasted temperature for the entire upper 3-m model area, side by side with remote sensing, AUV, and buoy measurements. The remote sensing data are filtered for quality and only compared to locations within the model domain (Figure 19b, orange area). Some days had full overcast (May 9, 2017) and therefore no remote sensing data are available. Some of the variations is related to difference in space, as the buoy is further inshore compared to the AUV, and time, because the AUV and remote sensing data were collected somewhat apart. However, there is a clear tendency of SINMOD to underestimate the surface temperature during the campaign; this is supported by both AUV data (Figure 14) and buoy time series (Figure 16).

6 | DISCUSSION

Our work shows the synergies to be exploited between data-driven sampling and synthetic ocean models, making oceanographic observations and data collection more efficient, by providing comparison of in-field data to augment and cross-validate model predictability, while also enabling greater capability to study and understand oceanographic processes and events. Using stochastic surrogate models, such as the GP model derived in this paper, allows the unification of both in situ measurements, data assimilation, and uncertainty quantification of the full hydrodynamic model, presenting scientists with a powerful framework for efficient experiment design.

As Zhang and Sukhatme (2007) pointed out, interpolation/kriging is required to estimate the value where no direct measurements are available; hence a bias is inevitable. Consequently, the algorithm will be exposed to high gradients as a result of failing to initialize the prior with

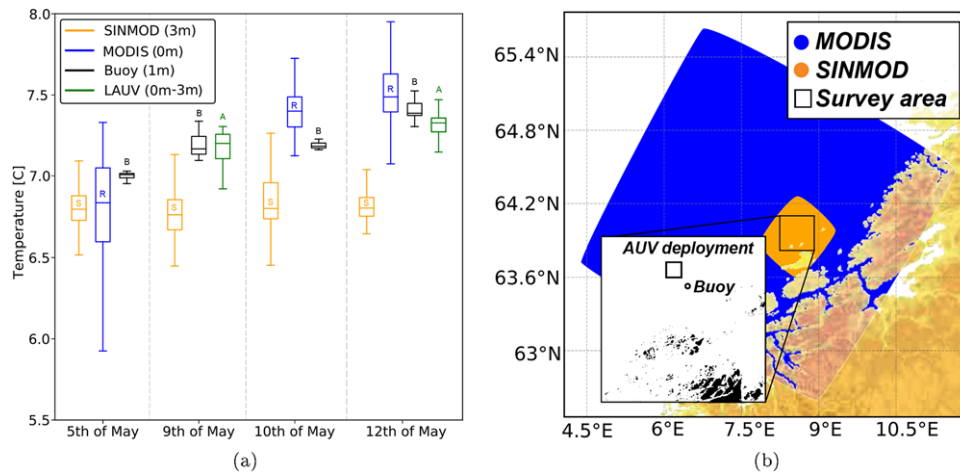


FIGURE 19 The 3-m water temperature nowcast from SINMOD compared to remote sensing SST products (MODIS), buoy measurements at 1 m depth, and AUV data from the surface layer 0–3 m, at noon. (a) Recorded temperatures at noon. S, R, B, and A denote SINMOD, remote sensing, buoy, and the AUV measurements, respectively. (b) Coverage and location map for the campaign at Froan (midway)

realistic values because prior and measured temperatures in unexplored locations typically deviate causing each update to generate a gradient peak that may not actually be realistic. Therefore, the objective function presented in this work counterbalances the gradient estimate with the corresponding uncertainty in P_{t,d_j} , while also performing a one-time-only bias correction of the prior mean estimate to avoid this effect.

Independent of the cost function, the algorithm used in this paper uses a one-step planning horizon, greedily choosing the path with the best objective value, for which an adverse effect can be attraction to local optima—there are a number of reasons for making this choice.

First, there are factors related to computational load, which grow exponentially for recursive approaches, originating from the combinatoric complexity as the graph network size increases. In the proposed approach, the graph is small and compute time is not an issue; however, as the method is devised for larger graphs, this is important to keep in mind, as some greedy-recursive approaches contemplate solutions shown to have better performance, see e.g., Ma, Liu, and Sukhatme (2016). So for larger graphs or limited computation, greedy approaches may provide “good enough” solutions (Binney et al., 2013) and acceptable performance, as shown in Krause et al. (2008). Second, as the methods used depend on ocean models, which are approximate, the inherent model uncertainty and integrated error effects will reduce the advantage gained in using a longer planning horizon. In some cases, this may cause the performance to become worse (Binney et al., 2013). The regional spatial and temporal scales on which to operate also come into consideration as upper water-column and coastal variability can neither be sampled nor modeled on a sustained and substantial basis (Lermusiaux, 2006). Some of these constraints can be managed; examples of nonmyopic approaches, such as Krause (2007) and Hoang, Low, Jaillet, and Kankanhalli (2014), can be used for active sampling, with complexity bounds on the exploration phase.

In terms of applicability, the end-to-end method presented in this work is general in the sense that the pipeline starting with (a) the discretization and spatial modeling of the phenomena using ocean model data, (b) formulation of the objective function toward a scientific con-

text, and (c) algorithmic implementation can easily be tailored to other environmental attributes or a combination of several, depending on the phenomena and scientific goals, where the perspective is the combination of ocean model data and in situ measurements. In our field experiment, both surveys showed a large variation with thermocline shift from 65 to 40 m, a spread in salinity from 33.0 to 34.9, and chlorophyll concentrations from 1 to 4 mg/m³. This observed variability across a range of environmental signatures demonstrates that using another type of environmental variable is possible and that to resolve different ocean phenomena measurements from several assets needs to be considered.

7 | CONCLUSIONS AND FUTURE WORK

In this work, we have presented methods for coupling ocean models with in situ data to achieve efficient sampling of coastal processes, with specific focus on the physical–biological coupling active in the Froan region, using ocean temperature as an information utility. Based on high-resolution hindcast data from the SINMOD ocean model, a stochastic proxy model using GPs was formulated, and a location-based covariance function was implemented to improve the assimilation of in situ measurements. To consolidate the GP model with the phenomena of interest for adaptive sampling, a variance and gradient-based objective function that accounts for uncertainty in the estimated gradients was established. The sampling algorithm, being both data- and model-driven, was tested in simulation and in sea trials, onboard an AUV. The experiments show that the algorithm differentiated between alternative survey strategies, having good agreement with model forecasts. The recorded data indicate correspondence between ocean model and AUV in determining a thermocline shift from influx of AW. Finally, we present supporting data from remote sensing, buoy, and ship-based measurements, and discuss how the combined data sources can be used improve ocean models.

Because only information from a specific depth region is utilized, we plan to extend the integration to several depths, which can be done

without significantly increasing the complexity of the system. This is also the case for extending the current GP model to include more complex spatiotemporal dynamics. A more advanced bias correction scheme will also be considered as several covariates and information sources can be included to contribute to augment the prior forecast coming from the model. Additionally, recursive approaches flanked by model or phenomena-based heuristics, which have a limited computational footprint, are also improvements that will be explored.

ACKNOWLEDGMENTS

This work was part of the ENTICE project funded by the Research Council of Norway Project #255303/E40,[#] the Nansen Legacy Program, project number #27272, and the AMOS, Center of Excellence funding scheme, project number #223254. We are grateful to the captain and crew of NTNU's research vessel, the R/V *Gunnerus*. We thank the anonymous reviewers for their insightful comments that significantly improved this paper. And finally, the authors are grateful for the support of João Sousa, João Pereira, Tiago Marques, and LSTS from the University of Porto, prior and subsequent to the field experiments in this work. LSTS' work was partially funded by the the European Union's Seventh Framework Programme (FP7/2007–2013) under grant agreement #270180 (NOPTILUS).

ORCID

Trygve Olav Fossum  <http://orcid.org/0000-0003-3468-9638>

REFERENCES

- Albretsen, J. (2011). *NorKyst-800 Report No. 1: User manual and technical descriptions*. Fiskeriet og havet. Bergen: Institute of Marine Research.
- Asplin, L., Salvanes, A. G. V., & Kristoffersen, J. B. (1999). Nonlocal wind-driven fjord-coast advection and its potential effect on plankton and fish recruitment. *Fisheries Oceanography*, 8(4), 255–263.
- Baafi, E., & Schofield, N. (1997). *Geostatistics*. *Geostatistics Wollongong'96*. Berlin: Springer Science and Business Media.
- Banerjee, S., Carlin, B. P., & Gelfand, A. E. (2014). *Hierarchical modeling and analysis for spatial data*. Boca Raton, FL: CRC Press.
- Barth, J. A., Hebert, D., Dale, A. C., & Ullman, D. S. (2004). Direct observations of along-isopycnal upwelling and diapycnal velocity at a shelfbreak front. *Journal of Physical Oceanography*, 34(3), 543–565.
- Bhattacharjya, D., Eidsvik, J., & Mukerji, T. (2013). The value of information in portfolio problems with dependent projects. *Decision Analysis*, 10(4), 341–351.
- Binney, J., Krause, A., & Sukhatme, G. S. (2010). Informative path planning for an autonomous underwater vehicle. *IEEE International Conference on Robotics and Automation* (pp. 4791–4796), Anchorage, Alaska.
- Binney, J., Krause, A., & Sukhatme, G. S. (2013). Optimizing waypoints for monitoring spatiotemporal phenomena. *International Journal of Robotics Research*, 32(8), 873–888.
- Broch, O. J., Ellingsen, I. H., Forbord, S., Wang, X., Volent, Z., Alver, M. O., ... Skjermo, J. (2013). Modelling the cultivation and bioremediation potential of the kelp *Sargassum latissima* in close proximity to an exposed salmon farm in Norway. *Aquaculture Environment Interactions*, 4(2), 187–206.
- Broch, O. J., Slagstad, D., & Smit, M. (2013). Modelling produced water dispersion and its direct toxic effects on the production and biomass of the marine copepod *Calanus finmarchicus*. *Marine Environmental Research*, 84(Supplement C), 84–95.
- Cao, N., Low, K. H., & Dolan, J. M. (2013). Multi-robot informative path planning for active sensing of environmental phenomena: A tale of two algorithms. *Proceedings of the 2013 International Conference on Autonomous Agents and Multi-agent Systems, AAMAS'13* (pp. 7–14), Richland, SC.
- Chang, D., Zhang, F., & Edwards, C. R. (2015). Real-time guidance of underwater gliders assisted by predictive ocean models. *Journal of Atmospheric and Oceanic Technology*, 32(3), 562–578.
- Chekuri, C., & Pal, M. (2005). A recursive greedy algorithm for walks in directed graphs. *46th Annual IEEE Symposium on Foundations of Computer Science, 2005, FOCS 2005* (pp. 245–253), Piscataway, NJ: IEEE.
- Cressie, N. A. C., & Wikle, C. K. (2011). *Statistics for spatio-temporal data*. *Probability and Statistics*. New York: Wiley.
- Curtin, T. B., Bellingham, J. G., Catipovic, J., & Webb, D. (1993). Autonomous oceanographic sampling networks. *Oceanography*, 6(3), 86–94.
- Das, J., Py, F., Harvey, J. B. J., Ryan, J. P., Gellene, A., Graham, R., ... Sukhatme, G. S. (2015). Data-driven robotic sampling for marine ecosystem monitoring. *International Journal of Robotics Research*, 34(12), 1435–1452.
- Das, J., Py, F., Maughan, T., Messie, M., O'Reilly, T., Ryan, J., ... Rajan, K. (2012). Coordinated sampling of dynamic oceanographic features with AUVs and drifters. *International Journal of Robotics Research*, 31, 626–646.
- Das, J., Rajan, K., Frolov, S., Ryan, J. P., Py, F., Caron, D. A., and Sukhatme, G. S. (2010). Towards marine bloom trajectory prediction for AUV mission planning. *IEEE International Conference on Robotics and Automation (ICRA)*, Anchorage, Alaska.
- Davis, R. A. (2014). *Gaussian process: Theory* (pp. 1–6). Hoboken, NJ: John Wiley & Sons.
- Donlon, C., Berruti, B., Buongiorno, A., Ferreira, M.-H., Féménias, P., Frerick, J., ... Sciarra, R. (2012). The global monitoring for environment and security (gmes) sentinel-3 mission. *Remote Sensing of Environment*, 120, 37–57.
- Eidsvik, J., Martinelli, G., & Bhattacharjya, D. (2018). Sequential information gathering schemes for spatial risk and decision analysis applications. *Stochastic Environmental Research and Risk Assessment*, 32(4), 1163–1177.
- Eidsvik, J., Mukerji, T., & Bhattacharjya, D. (2015). *Value of information in the earth sciences: Integrating spatial modeling and decision analysis*. Cambridge: Cambridge University Press.
- Ellingsen, I., Dalpadado, P., Slagstad, D., & Loeng, H. (2008). Impact of climatic change on the biological production in the Barents Sea. *Climate Change*, 87(1), 155–175.
- Ellingsen, I., Slagstad, D., & Sundfjord, A. (2009). Modification of water masses in the Barents Sea and its coupling to ice dynamics: A model study. *Ocean Dynamics*, 59(6), 1095–1108.
- Forristall, G. (2011). *Lofoten and Vesteralen currents (LOVECUR): Comparison of hindcasts with measurements* (Technical report). Camden, ME: Forristall Ocean Engineering, Inc.
- Franks, P. J. S. (1992). Sink or swim: Accumulation of biomass at fronts. *Marine Ecology Progress Series*, 82, 1–12.
- Frolov, S., Paduan, J., Cook, M., & Bellingham, J. (2012). Improved statistical prediction of surface currents based on historic HF-radar observations. *Ocean Dynamics*, 62(7), 1111–1122.
- Gordoa, A., Masó, M., & Voges, L. (2000). *Satellites, oceanography and society* (Vol. 63). Amsterdam: Elsevier Science.

[#] <https://www.sintef.no/en/projects/entice/>.

- Graham, R., Py, F., Das, J., Lucas, D., Maughan, T., & Rajan, K. (2012). Exploring space-time tradeoffs in autonomous sampling for marine robotics. *International Symposium on Experimental Robotics (ISER)*, Quebec City, Canada.
- Guestrin, C., Krause, A., & Singh, A. P. (2005). Near-optimal sensor placements in Gaussian processes. *Proceedings of the 22nd International Conference on Machine Learning* (Vol. 1, pp. 1–8).
- Hoang, T. N., Low, B. K. H., Jaillet, P., & Kankanhalli, M. (2014). Nonmyopic ϵ -Bayes-optimal active learning of Gaussian processes. *International Conference on Machine Learning* (pp. 739–747).
- Holt, J. T., Allen, J. I., Proctor, R., & Gilbert, F. (2005). Error quantification of a high-resolution coupled hydrodynamic-ecosystem coastal-ocean model: Part 1 model overview and assessment of the hydrodynamics. *Journal of Marine Systems*, 57(1), 167–188.
- Howe, B. M., Chao, Y., Arabshahi, P., Roy, S., McGinnis, T., & Gray, A. (2010). A smart sensor web for ocean observation: Fixed and mobile platforms, integrated acoustics, satellites and predictive modeling. *IEEE Journal of Selected Topics in Applied Earth Observations and Remote Sensing*, 3(4), 507–521.
- Ikeda, M., Johannessen, J. A., Lygre, K., & Sandven, S. (1989). A process study of mesoscale meanders and eddies in the Norwegian coastal current. *Journal of Physical Oceanography*, 19(1), 20–35.
- Krause, A. (2007). Nonmyopic active learning of Gaussian processes: An exploration–exploitation approach. *Proceedings of the IEEE International Conference on Machine Learning* (pp. 449–456), Pittsburgh, PA.
- Krause, A., Guestrin, C., Gupta, A., & Kleinberg, J. (2006). Near-optimal sensor placements: maximizing information while minimizing communication cost. *2006 5th International Conference on Information Processing in Sensor Networks* (pp. 2–10), Nashville, TN.
- Krause, A., Singh, A., & Guestrin, C. (2008). Near-optimal sensor placements in Gaussian processes: Theory, efficient algorithms and empirical studies. *Journal of Machine Learning Research*, 9, 235–284.
- Leonard, N. E., Paley, D. A., Lekien, F., Sepulchre, R., Fratantoni, D. M., & Davis, R. E. (2007). Collective motion, sensor networks, and ocean sampling. *Proceedings of the IEEE*, 95(1), 48–74.
- Lermusiaux, P. F. J. (2006). Uncertainty estimation and prediction for interdisciplinary ocean dynamics. *Journal of Computational Physics*, 217(1), 176–199.
- Lévy, M. (2003). Mesoscale variability of phytoplankton and of new production: Impact of the large-scale nutrient distribution. *Journal of Geophysical Research: Oceans*, 108(C11). <https://doi.org/10.1029/2002JC001577>.
- Ling, C. K., Low, K. H., & Jaillet, P. (2016). Gaussian process planning with Lipschitz continuous reward functions: Towards unifying Bayesian optimization, active learning, and beyond. *Proceedings Association for the Advancement of Artificial Intelligence* (pp. 1860–1866), Phoenix, AZ.
- Low, K. H., Dolan, J. M., & Khosla, P. (2011). Active Markov information-theoretic path planning for robotic environmental sensing. *The 10th International Conference on Autonomous Agents and Multiagent Systems, AAMAS'11* (Vol. 2, pp. 753–760), Taipei, Taiwan.
- Ma, K.-C., Liu, L., & Sukhatme, G. S. (2016). An information-driven and disturbance-aware planning method for long-term ocean monitoring. *2016 IEEE/RSJ International Conference on Intelligent Robots and Systems (IROS)* (pp. 2102–2108). Piscataway, NJ: IEEE.
- Marchant, R., Ramos, F., Sanner, S., et al. (2014). Sequential Bayesian optimization for spatial-temporal monitoring. *Proceedings Uncertainty in Artificial Intelligence* (pp. 553–562), Quebec City, Quebec.
- Matérn, B. (2013). Spatial variation. *Meddelanden från Statens Skogsforskningsinstitut*, 36(5), 1–144.
- Minnett, P., & Kaiser-Weiss, A. (2012). Near-surface oceanic temperature gradients (GHRSS Discussion Doc).
- Moses, W. J., Ackleson, S. G., Hair, J. W., Hostetler, C. A., & Miller, W. D. (2016). Spatial scales of optical variability in the coastal ocean: Implications for remote sensing and in situ sampling. *Journal of Geophysical Research: Oceans*, 121(6), 4194–4208.
- Müller, M., Homleid, M., Ivarsson, K.-I., Kjøltzow, M. A., Lindskog, M., Midtbø, K. H., ... Vignes, O. (2017). Arome-metcoop: A nordic convective-scale operational weather prediction model. *Weather and Forecasting*, 32(2), 609–627.
- Pinto, J., Calado, P., Braga, J., Dias, P., Martins, R., Marques, E., & Sousa, J. (2012). Implementation of a control architecture for networked vehicle systems. *IFAC Proceedings Volumes*, 45(5), 100–105.
- Pinto, J., Diasand, P. S., Martins, R., Fortuna, J., Marques, E., & Sousa, J. (2013). The LSTS toolchain for networked vehicle systems. *MTS/IEEE Oceans* (pp. 1–9). Piscataway, NJ: IEEE.
- Py, F., Rajan, K., & McGann, C. (2010). A systematic agent framework for situated autonomous systems. *International Conference on Autonomous Agents and Multiagent Systems (AAMAS)*, Toronto, Canada.
- Rajan, K., & Py, F. (2012). T-REX: Partitioned inference for AUV mission control. In G. N. Roberts & R. Sutton (Eds.), *Further advances in unmanned marine vehicles*. Michael Faraday House, Stevenage: The Institution of Engineering and Technology (IET).
- Rajan, K., Py, F., & Berreiro, J. (2012). Towards deliberative control in marine robotics. In M. Seto (Ed.), *Marine robot autonomy*. Berlin: Springer.
- Ramp, S. R., Davis, R. E., Leonard, N. E., Shulman, I., Chao, Y., Robinson, A. R., ... Li, Z. (2009). Preparing to predict: The Second Autonomous Ocean Sampling Network (AOSN-II) experiment in the Monterey Bay. *Deep-Sea Research Part II: Topical Studies in Oceanography*, 56(3-5), 68–86.
- Rao, D., & Williams, S. B. (2009). Large-scale path planning for underwater gliders in ocean currents. *Australasian Conference on Robotics and Automation (ACRA)*, Sydney.
- Sætre, R. (1999). Features of the central norwegian shelf circulation. *Continental Shelf Research*, 19(14), 1809–1831.
- Sætre, R. (2007). *The Norwegian coastal current: Oceanography and climate*. Bergen: The Institute of Marine Research, Tapir Academic Press.
- Sakov, P., & Oke, P. R. (2008). Objective array design: Application to the tropical indian ocean. *Journal of Atmospheric and Oceanic Technology*, 25(5), 794–807.
- Sakshaug, E., Johnsen, G., & Kovacs, K. (2009). *Ecosystem Barents Sea. Physical oceanography*. Trondheim: Tapir Academic Press.
- Savtchenko, A., Ouzounov, D., Ahmad, S., Acker, J., Leptoukh, G., Koziana, J., & Nickless, D. (2004). Terra and Aqua MODIS products available from NASA GES DAAC. *Advances in Space Research*, 34(4), 710–714.
- Shchepetkin, A. F., & McWilliams, J. C. (2005). The regional oceanic modeling system (ROMS): A split-explicit, free-surface, topography-following-coordinate oceanic model. *Ocean Modelling*, 9(4), 347–404.
- Singh, A., Krause, A., Guestrin, C., & Kaiser, W. J. (2009). Efficient informative sensing using multiple robots. *Journal of Artificial Intelligence Research*, 34, 707–755.
- Skarøhamar, J., Slagstad, D., & Edvardsen, A. (2007). Plankton distributions related to hydrography and circulation dynamics on a narrow continental shelf off Northern Norway. *Estuarine, Coastal and Shelf Science*, 75(3), 381–392.
- Slagstad, D., & McClimans, T. A. (2005). Modeling the ecosystem dynamics of the Barents Sea including the marginal ice zone: I. Physical and chemical oceanography. *Journal of Marine Systems*, 58(1–2), 1–18.
- Slagstad, D., Wassmann, P. F., & Ellingsen, I. (2015). Physical constrains and productivity in the future arctic ocean. *Frontiers in Marine Science*, 2, 85.
- Smith, R. N., Das, J., Yi, C., Caron, D. A., Jones, B. H., & Sukhatme, G. S. (2010). *Cooperative multi-AUV tracking of phytoplankton blooms based on ocean model predictions*. Sydney: IEEE Oceans.

- Smith, R. N., Py, F., Cooksey, P., Sukhatme, G., & Rajan, K. (2016). *Adaptive path planning for tracking ocean fronts with an autonomous underwater vehicle*. Morocco: International Symposium on Experimental Robotics (ISER).
- Smith, R. N., Schwager, M., Smith, S. L., Jones, B. H., Rus, D., & Sukhatme, G. S. (2011). Persistent ocean monitoring with underwater gliders: Adapting sampling resolution. *Journal of Field Robotics*, 28(5), 714–741.
- Sousa, A., Madureira, L., Coelho, J., Pinto, J., Pereira, J., Sousa, J., and Dias, P. (2012). LAUV: The man-portable autonomous underwater vehicle. Navigation, Guidance and Control of Underwater Vehicles (Vol. 3, pp. 268–274). <https://doi.org/10.3182/20120410-3-PT-4028.00045>.
- Stein, M. L. (2005). *Nonstationary spatial covariance functions (CISES Technical Report 21)*. Chicago, IL: University of Chicago.
- Stein, M. L., Chi, Z., & Welty, L. J. (2004). Approximating likelihoods for large spatial data sets. *Journal of the Royal Statistical Society: Series B (Statistical Methodology)*, 66(2), 275–296.
- Stewart, R. (2009). *Introduction to physical oceanography*. Gainesville, FL: University Press of Florida.
- Sverdrup, K. A., Duxbury, A., & Duxbury, A. C. (2006). *Fundamentals of oceanography*. New York: McGraw-Hill Higher Education.
- Trenberth, K. (1992). *Climate system modeling*. Cambridge: Cambridge University Press.
- Troccoli, A. (2003). *A proposal for correcting the wind stress forcing of an ocean model*. Nice, France: EGS-AGU-EUG Joint Assembly.
- Vanhellemont, Q., & Ruddick, K. (2016). Acolite for sentinel-2: Aquatic applications of MSI imagery. *Proceedings of the ESA Living Planet Symposium* (pp. 9–13), Prague, Czech Republic.
- Wassmann, P., Slagstad, D., & Ellingsen, I. (2010). Primary production and climatic variability in the European sector of the arctic ocean prior to 2007: Preliminary results. *Polar Biology*, 33(12), 1641–1650.
- Wassmann, P., Slagstad, D., Riser, C. W., & Reigstad, M. (2006). Modelling the ecosystem dynamics of the Barents Sea including the marginal ice zone: II. *Carbon flux and interannual variability*. *Journal of Marine Systems*, 59(1–2), 1–24.
- Werdell, P. J., & Bailey, S. W. (2005). An improved in-situ bio-optical data set for ocean color algorithm development and satellite data product validation. *Remote Sensing of Environment*, 98(1), 122–140.
- Wunsch, C., & Heimbach, P. (2007). Practical global oceanic state estimation. *Physica D: Nonlinear Phenomena*, 230(1–2), 197–208.
- Yilmaz, N. K., Evangelinos, C., Lermusiaux, P. F., & Patrikalakis, N. M. (2008). Path planning of autonomous underwater vehicles for adaptive sampling using mixed integer linear programming. *IEEE Journal of Oceanic Engineering*, 33(4), 522–537.
- Zamuda, A., Hernandez Sosa, J. D., & Adler, L. (2016). Constrained differential evolution optimization for underwater glider path planning in sub-mesoscale eddy sampling. *Applied Soft Computing*, 42, 93–118.
- Zhang, B., & Sukhatme, G. S. (2007). Adaptive sampling for estimating a scalar field using a robotic boat and a sensor network. *Proceedings 2007 IEEE International Conference on Robotics and Automation* (pp. 3673–3680), Piscataway, NJ: IEEE.
- Zhang, B., Sukhatme, G. S., & Requicha, A. A. (2004). Adaptive sampling for marine microorganism monitoring. *Proceedings Intelligent Robots and Systems (IROS)* (Vol. 2, pp. 1115–1122). Piscataway, NJ: IEEE.

How to cite this article: Fossum TO, Eidsvik J, Ellingsen I, Alver MO, Fragoso GM, Johnsen G, Mendes R, Ludvigsen M, Rajan K. Information-driven robotic sampling in the coastal ocean. *J Field Robotics*. 2018;1–21. <https://doi.org/10.1002/rob.21805>